**Forthcoming Articles** have been peer-reviewed and accepted for publication in *InterPore Journal*. To make research available as early as possible, accepted manuscripts may be published online prior to completion of the final production process. These versions have not yet undergone final formatting, proofreading, or author corrections and therefore do not represent the **Version of Record**. Minor changes may occur during the final production process. The article will be updated with the final Version of Record when it is published in its assigned journal issue. **Forthcoming Articles should be cited using their DOI, which will remain the same after publication of the final Version of Record.**

**Please cite the following article as:**

Rahnamaybahambary, K., Jain, T. K., Sahu, C. K., & Flynn, M. (2026). DOUBLE-DIFFUSIVE GRAVITY CURRENTS IN POROUS MEDIA – IMPLICATIONS FOR APPLYING DENSITY COMPENSATION IN AQUIFER THERMAL ENERGY STORAGE SYSTEMS. *InterPore Journal*. Forthcoming Article.
https://doi.org/10.69631/6k8t6965

**Received on:** 05 May 2026
**Accepted on:** 06 Oct. 2026
**Published online (Accepted version):** 30 Oct. 2026

InterPore JOURNAL

Original Research

# DOUBLE-DIFFUSIVE GRAVITY CURRENTS IN POROUS MEDIA – IMPLICATIONS FOR APPLYING DENSITY COMPENSATION IN AQUIFER THERMAL ENERGY STORAGE SYSTEMS

K RahnamayBahambary[1], Tarun K. Jain[1 2], Chunendra K. Sahu[2], M. R. Flynn[1]

[1]*Dept. of Mechanical Engineering, U. Alberta, Edmonton, AB, Canada, T6G 1H9;* [2]*Dept. of Civil Engineering, Indian Institute of Technology, Kanpur-208016, Uttar Pradesh, India;*

**Correspondence to:**
Khashayar RahnamayBahambary,
krahnama@ualberta.ca

**How to Cite:**
This information will be updated by the Editorial Office once the article is ready to be published.
https://doi.org/10.69631/xxxxxxx

**RECEIVED:** 00 Month 0000
**ACCEPTED:** 01 Month 0000
**PUBLISHED:** 02 Month 0000

## ABSTRACT

To improve the efficiency of aquifer thermal energy storage (ATES) systems, it is desirable to minimize the spreading of the buoyant injected fluid. One proposed approach is density compensation, whereby a solute like salt is added to the injectate to increase its density and reduce buoyancy-driven spreading. This study investigates the physics of double-diffusive porous media gravity currents and thereby assesses, from a small-scale fluid mechanical point of view, the benefits and drawbacks of such density compensation. Accordingly, we perform direct numerical simulations of hot and salty into cold and fresh lock-exchange flows in the Boussinesq limit. Numerical output shows that the dynamics of double-diffusive gravity currents differ markedly from their single-diffusive counterparts. For instance, where convective instabilities, i.e, fingers, occur, they have the effect of increasing the speed of propagation and therefore increasing rates of mixing and spreading. Whereas similar observations have been made in the context of double-diffusive gravity currents in free media (c.f. Konopliv and Meiburg, *J. Fluid Mech.*, **797**, 729-764, 2016), the inclusion of the porous medium introduces fundamentally new effects because, for example, the medium can entrap heat but not salt. Moreover, porosity is a dynamically-significant variable because instability onset is retarded in tight media. Overall, the findings suggest that although density compensation slows gravity current spread in an ATES context, its effectiveness depends on suppressing fingering instabilities; hence, slightly salting the injectate to ensure a density greater than that of the native aquifer fluid is recommended.

## KEYWORDS

Double-diffusive convection, Porous media gravity currents, Aquifer thermal energy systems

© 2026 The Authors

This is an open access article published by InterPore under the terms of the Creative Commons Attribution-NonCommercial-NoDerivatives 4.0 International License (CC BY-NC-ND 4.0) (https://creativecommons.org/licenses/by-nc-nd/4.0/).

# 1. INTRODUCTION

Within the building/industrial heating sector, the need for a rapid shift away from fossil fuel-based combustion systems has drastically increased interest in seasonal aquifer thermal energy storage (ATES) [24]. In open-loop ATES systems, warm water is injected underground during summer months and stored in underground aquifers to be used for heating in the winter. To minimize the lateral spreading of the injected hot water and its mixing with ambient fluid within the aquifer, the temperature difference between the two fluids should be less than 20°C [1]. However, to enhance the energy yield of ATES systems, designs employing temperature differences as large as 70°C have been proposed [4]. Accordingly, an open question is whether high-temperature ATES systems can be devised that avoid the loss of efficiency associated with the migration of the hot water plume. One possible remedy, explored in quantitative detail by [22], is to apply density-compensation by which salt is added to the injectate to increase its density, thereby reducing buoyancy-driven spreading underground. While their study demonstrated that this approach could, in theory, improve efficiency by up to 30%, the analysis did not account for double-diffusive effects and the convective instabilities associated thereto.

Convective instabilities play a central role in a wide range of environmental and geophysical processes [20]. Such instabilities occur both in free fluids—for example, thermo-haline instabilities in the ocean [19, 16] and in porous media, such as during enhanced oil recovery or $CO_2$ sequestration [7]. In the latter case, in particular, fingering instabilities commonly occur. Though the fingers associated with hydrocarbon production or $CO_2$ sequestration derive from injecting a less viscous fluid into a more viscous one inside a porous medium, thereby producing the classical Saffman–Taylor instability [7], fingers may also arise because of the unstable stratification of an active scalar. Such is the origin of the fingers associated with double-diffusive convection, where there appear two scalars (such as heat and salt[1]) that diffuse at different rates [21]. Importantly, a fingering instability, though especially important to this particular study, is not the only instability that can arise in a double-diffusive system, whether or not characterized by the presence of a porous medium. Rather, the particulars of the flow field depend on the relative distribution of heat and salt across the fluid layers [10]. When cold, fresh fluid overlies hot, salty fluid, layers rather than fingers are anticipated. By contrast, fingers appear when hot, salty fluid overlies cold fresh fluid [16].

The physics of double-diffusive convective instabilities in the context of a stationary base state have been extensively studied in both free [19, 21] and porous media [12, 5]. Such stationary base states arise when the hot/salty and cold/fresh fluids are separated by an interface that is initially horizontal. Making the interface vertical introduces fundamentally new dynamics because of the formation of counter-flowing gravity currents whose propagation influences instability development and vice-versa. These details were explored in a free medium context by Konopliv and Meiburg, who carried out a detailed numerical investigation of double-diffusive convection in a lock-release configuration. More specifically, Konopliv and Meiburg [9] showed that fingering enhances the mixing of both the faster-diffusing scalar (heat) and the slower-diffusing scalar (salt), while also increasing the gravity current front speed. Insightful as their study was, it is unclear the extent to which the results of Konopliv and Meiburg [9] can be extended to

[1]Sarkar & Phillips [17, 18] argue that porous media flows characterized by convective instabilities arising from the presence of heat and salt are more often driven by double-*advective* than double-*diffusive* effects. For terminological simplicity and to facilitate a comparison with related free-medium studies, e.g. Konopliv and Meiburg [9], we retain the term 'double-diffusive' but acknowledge that the presence of the solid medium causes temperature perturbations to advect more slowly than their saline counterparts. When considering diffusive transport, the direction of the inequality is, of course, reversed [15].

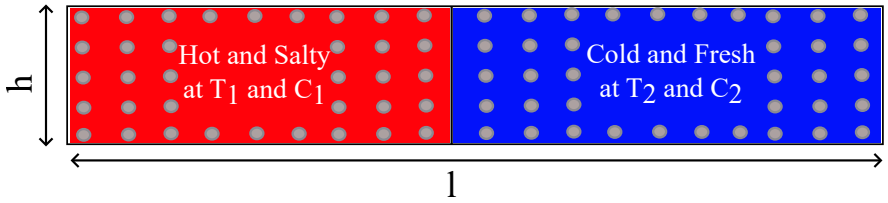



**Figure 1:** The simulation domain where $l = 2\,\mathrm{m}$ and $h = 0.2\,\mathrm{m}$. The vertical interface separating the hot/salty and cold/fresh fluids is situated along the mid-plane.

porous media gravity currents. For one, flows inside porous media are almost always laminar as compared to the high Reynolds number simulations performed by Konopliv and Meiburg [9]. Moreover, the porous medium entraps heat but not salt—a consequence of the local thermal equilibrium between the fluid and solid phases, discussed further in Section 2—and therefore the dynamical importance of one versus the other scalar is fundamentally different from that in the free medium circumstance. These differences, and the open questions that follow from said differences, motivate the present study. In turn, we aspire to provide suggestive insights into the operation of density-compensated ATES systems. Our analysis applies direct numerical simulations of double-diffusive lock-exchange flows across a wide range of initial conditions and thereby quantifies the extent to which double diffusion alters the dynamics of gravity currents in porous media.

The remainder of this paper presents the numerical methodology, governing equations, and parameter space (Section 2), followed by results highlighting the effects of fluid properties (Section 3) and porous-medium characteristics (Section 4). We conclude by summarizing implications for density-compensation strategies in ATES systems (Section 5).

# 2. PROBLEM DESCRIPTION

We numerically simulate a lock-exchange configuration in which hot/salty and cold/fresh fluids occupy the left- and right-hand sides of a rectilinear domain, respectively, at the initial time $t = 0$, as shown in figure 1. This idealized geometry is adopted as a tractable surrogate for ATES injection scenarios: while this configuration does not replicate the radial geometry or well-driven flow of a real system, it isolates the density-driven dynamics governing buoyancy-induced mixing in a systematic and physically-transparent manner. The lessons drawn regarding the role of salinity in compensating for adverse thermal density differences are therefore expected to carry over to realistic injection and withdrawal conditions. The hot and salty fluid is initialized with temperature $T_1$ and salinity $C_1$, while the cold and fresh fluid is assigned initial conditions $T_2 = 293$ K and $C_2 = 0$ mol/m$^3$. The resulting problem is an initial-boundary-value problem, in which the temperature, salinity, and velocity fields evolve as functions of both space and time from the prescribed initial state subject to the domain boundary conditions specified in the following. The equations of motion are solved assuming a domain length of $l = 2\,\mathrm{m}$ and a height of $h = 0.2\,\mathrm{m}$. Although 2D numerical simulations cannot capture the full three-dimensionality of convective fingers in a high Rayleigh number regime [6], they provide an accurate description of the gravity current length, notably in cases with low lateral aspect ratio [11]. Furthermore, for all the simulations conducted herein, the Darcy-Rayleigh number is small enough that we never realize turbulent flows for which 3D numerical simulations would be required.

## 2.1. Theory

The dimensional and non-dimensional forms of the governing equations are first presented to facilitate a better understanding of the parameter space relevant to the flow in question. It must be noted that COMSOL Multiphysics solves the dimensional form of the equations, and the nondimensional form is presented here to help formulate the problem in a more systematic manner and to define the parameter space that governs the double-diffusive lock-exchange setup. By invoking the Boussinesq approximation,

the dimensional forms of the mass, momentum, and scalar transport equations are as follows:

$$\varepsilon\frac{\partial\rho}{\partial t}+\nabla\cdot(\rho\boldsymbol{u})=0 \tag{1}$$

$$\boldsymbol{u}=-\frac{\kappa}{\mu}\left(\nabla p-\rho\mathbf{g}\right) \tag{2}$$

$$G\frac{\partial T}{\partial t}+\boldsymbol{u}\cdot\nabla T=\alpha_e\nabla^2 T \tag{3}$$

$$\varepsilon\frac{\partial C}{\partial t}+\boldsymbol{u}\cdot\nabla C=D_e\nabla^2 C \tag{4}$$

Here $\varepsilon$ and $\kappa$ are the medium porosity and permeability, respectively, $\mu$ is the dynamic viscosity, $\rho$ is the fluid density, $\boldsymbol{u}$ is the fluid velocity, $c$ is the solute concentration and $T$ is the temperature, which we assume to be identical for both solid and fluid at any particular point in space. Meanwhile, $\alpha_e$ is the effective thermal diffusivity, defined as

$$\alpha_e=\frac{1}{(\rho C_P)_f}\left[\varepsilon k_f+(1-\varepsilon)k_s\right] \tag{5}$$

where $k$ and $C_p$ respectively denote the thermal conductivity and specific heat capacity at constant pressure; the subscripts $f$ and $s$ respectively indicate 'fluid' and 'solid.' Furthermore, $D_e$ is the effective mass diffusivity, defined as

$$D_e=\varepsilon D_c \tag{6}$$

where $D_c$ is the solute mass diffusivity. Finally,

$$G=\frac{(\rho C_p)_m}{(\rho C_p)_f}\qquad\text{where}\qquad(\rho C_P)_m=\varepsilon(\rho C_p)_f+(1-\varepsilon)(\rho C_p)_s \tag{7}$$

In calculating fluid densities, we consider a linear equation of state such that

$$\rho=\rho_0[1+\beta(C-C_{\text{ref}})-\alpha(T-T_{\text{ref}})] \tag{8}$$

Here $\beta$ is the saline contraction coefficient, $\alpha$ is the thermal expansion coefficient, and $C_{\text{ref}}=0$ and $T_{\text{ref}}=T_2$ are the reference salinity (expressed in units of $\text{mol/m}^3$) and temperature, respectively.

To derive the nondimensional form of the governing equations, we restrict attention to incompressible flow; (1) can be replaced by $\nabla\cdot\boldsymbol{u}=0$. Furthermore, the hydrostatic pressure contribution, $\rho_0 g$, can be incorporated into the $\nabla p$ term in (2) such that $\tilde{P}=p+\rho_0 gz$, where $\tilde{P}$ is the hydrostatically-adjusted pressure. Expanding our focus to additionally include (3-4) and applying the following characteristic scales:

$$\boldsymbol{x}=h\boldsymbol{x}^* \tag{9}$$

$$\boldsymbol{u}=U_f\boldsymbol{u}^* \tag{10}$$

$$t=\frac{h}{U_f}t^* \tag{11}$$

$$\tilde{P}=\frac{\mu U_f h}{\kappa}P^* \tag{12}$$

$$T=T_1+T^*\Delta T_0 \tag{13}$$

$$C=C_1+C^*\Delta C_0 \tag{14}$$

allows us to recast (1-4) in non-dimensional form. Here, starred variables carry no units. Moreover, $\Delta C_0$ and $\Delta T_0$ respectively correspond to the initial differences of salinity and temperature of the fluids on either side of the vertical interface in figure 1. Finally, $U_f$ is a representative gravity current speed whose precise definition will be provided in Section 3.1. Thus do we find that

$$\mathrm{Pe}\,\boldsymbol{u}^* = -\mathrm{Pe}\,\nabla^* P^* - \mathrm{Da}\,(\mathrm{Ra}_C C^* - \mathrm{Ra}_T T^*)\mathbf{k} \tag{15}$$

$$G\frac{\partial T^*}{\partial t^*} + \boldsymbol{u}^* \cdot \nabla^* T^* = \frac{1}{\mathrm{Pe}}\nabla^{*2} T^* \tag{16}$$

$$\varepsilon\frac{\partial C^*}{\partial t^*} + \boldsymbol{u}^* \cdot \nabla^* C^* = \frac{1}{\mathrm{Le}\,\mathrm{Pe}}\nabla^{*2} C^* \tag{17}$$

where Pe is the Péclet number, Da is the Darcy number, $\mathrm{Ra}_T$ and $\mathrm{Ra}_C$ are the thermal and saline Reyleigh numbers, respectively, Le is the Lewis number and the unit vector $\mathbf{k}$ is defined as $\mathbf{k} = (0, 1)$. The aforementioned non-dimensional variables are given by

$$\mathrm{Pe} = \frac{hU_f}{\alpha_e} \tag{18}$$

$$\mathrm{Da} = \frac{\kappa}{h^2} \tag{19}$$

$$\mathrm{Ra}_T = \frac{\rho_0 g h^3 \alpha \Delta T}{\mu \alpha_e} \tag{20}$$

$$\mathrm{Ra}_C = \frac{\rho_0 g h^3 \beta \Delta C}{\mu \alpha_e} \tag{21}$$

$$\mathrm{Le} = \frac{\alpha_e}{D_e} \tag{22}$$

Note that the product $\mathrm{Da}\,\mathrm{Ra}$ is often denoted by $\mathrm{Ra}_D$ and referred to as the Rayleigh-Darcy number. We do not adopt this notation here to avoid a cumbersome jumble of subscripts, i.e. $\mathrm{Ra}_{D,T}$ and $\mathrm{Ra}_{D,C}$.

## 2.2. Numerical methodology

To solve the aforementioned equations numerically, direct numerical simulations are performed using COMSOL Multiphysics, which requires consideration of dimensional variables and equations. For all parameter combinations, numerical simulations are run for a dimensional time of 90 min. Numerical values for the constants $\kappa$, $\varepsilon$, etc. used in the simulations can be found in Table 1. Absent from this table is the dynamic viscosity, which is calculated using a built-in function that employs a sixth-degree polynomial in temperature. A structured grid with a grid spacing of 2.5 mm with additional near-wall refinement, corresponding to a resolution of approximately $90 \times 900$, is used to discretize the domain. We verified that our results were grid-independent by considering five additional grid resolutions with spacings of $[1.6, 2.0, 3.0, 4.3, 5.0]$ mm. From the numerical data collected using these grids, grid independence was formally confirmed using the analysis presented in Appendix A.

In the absence of experimental or theoretical results for the double-diffusive configuration considered here, the numerical framework was validated against a reduced, single-diffusive analogue in which the density contrast arises from salinity alone. A full-depth lock exchange of fresh against saline water was simulated in the same confined porous layer shown in figure 1. The resulting interface evolution was compared with the sharp-interface, depth-integrated model of section 5 of Huppert and Woods (1995). When the ambient and injectate have the same viscosity, this model admits a closed-form similarity solution in which the elongating interface is a sloping line that pivots about the gate midpoint. Meanwhile, the two contact lines propagate according to $\ell = (UHt)^{1/2}$, where $U = k\Delta\rho g/\mu\phi$ is the buoyancy velocity. As seen from

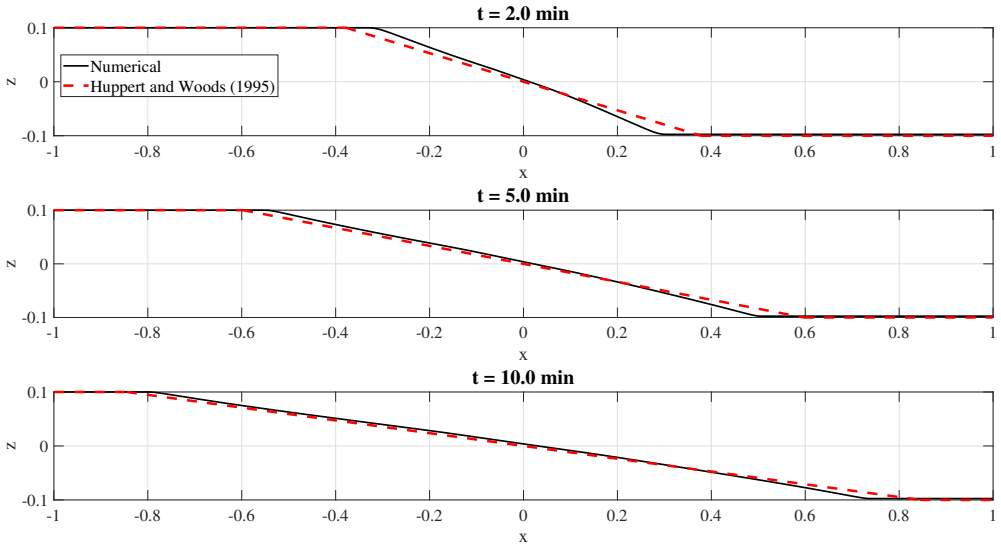



**Figure 2:** Gravity current interface of the numerical and theoretical sharp interface model for the single diffusive case.

figure 2, both the interface profiles and the front positions obtained from the present simulations agree closely with this solution, with departures confined to the immediate vicinity of the two noses, where the diffuse interface resolved by the full Darcy solution deviates from the sharp-interface idealization. This agreement builds confidence in the numerical framework before applying it to the double-diffusive problem.

As noted earlier in conjunction with (15-17), the non-dimensional numbers governing the flow evolution are Pe, $\mathrm{Da}\,\mathrm{Ra}_T$, $\mathrm{Da}\,\mathrm{Ra}_C$, Le, $G$, and $\varepsilon$. The main goal of this study is to characterize the dynamical evolution of gravity currents generated by lock exchange in terms of these non-dimensional variables. To this end, the first sub-section below (3.1) studies gravity current propagation for different values of the saline and thermal Rayleigh numbers. In calculating particular values for $\mathrm{Ra}_C$ and $\mathrm{Ra}_T$, we return to figure 1 and note that the initial configuration includes cold and fresh fluid with an assumed temperature of $T_2 = 293\,\mathrm{K}$ and a density of $\rho_2 = 1000\,\mathrm{kg/m^3}$. Meanwhile, to the left of the vertical interface (or "lock gate"), we consider various values for $T_1$ and $C_1$ and, by extension, for the stability ratio, $N = \mathrm{Ra}_C/\mathrm{Ra}_T$. More specifically, we consider five different values for $T_1$ and five different values for $C_1$ and hence our non-dimensional parameter space is as depicted in figure 3. In this figure, the line $N = 1$ is highlighted because the stability ratio is an important parameter that dictates the type of convective instability to be realized for $t > 0$. When $N < 1$ (corresponding to the region below the diagonal line in figure 3), the hot/salty fluid flows over the cold/fresh fluid and the flow regime is "finger-favourable." Conversely, when $N > 1$, fluid instabilities are expected to result not in the formation of convective fingers but rather of horizontal layers [10]. Values of $N$ corresponding to the 25 data points of figure 3 are given in table 2. Also specified in table 2 are the associated dimensional values for $T_1$, $C_1$, and $\rho_1$. Furthermore, table 2 gives the value for the initial density contrast, $\Delta\rho$, between the left- and right-hand sides of the tank where $\Delta\rho > 0$ indicates that $\rho_1 > \rho_2$, i.e. that the density of the hot and salty fluid exceeds that of the cold and fresh fluid. The final three columns of table 2 specify the numerical values of key non-dimensional variables, i.e. $N$, $\mathrm{Da}\,\mathrm{Ra}_T$ and $\mathrm{Da}\,\mathrm{Ra}_C$.

# 3. EFFECTS OF FLUID PROPERTIES

## 3.1. Finger-favourable regime, $N < 1$

Our analysis begins with an examination of the double-diffusive convective instabilities that arise when hot and salty fluid overlies fluid that is cold and fresh. The temperature and salinity distributions after

**Table 1:** Numerical values for the constants appearing in equations (1-8). For convenience, the heat conductivities of the solid and fluid phases are assumed equal. By this choice, the porosity sensitivity study conducted in Section 4.1 does not consider the medium effective thermal diffusivity as a key dynamical variable, see (5).

| Parameter | Value |
|---|---|
| $\kappa$ | $10^{-8}$ m$^2$ |
| $\varepsilon_1$ | 0.33 |
| $\rho_s$ | 2000 kg/m$^3$ |
| $\rho_f = \rho_0$ | 1000 kg/m$^3$ |
| $C_{ps}$ | 2100 J/kg.K |
| $C_{pf}$ | 4200 J/kg.K |
| $k_f$ | 0.6 W/m.K |
| $k_s$ | 0.6 W/m.K |
| $D_c$ | $1.5\times10^{-9}$ m$^2$/s |
| $\alpha$ | $5\times10^{-4}$ 1/K |
| $\beta$ | $5\times10^{-5}$ m$^3$/mol |

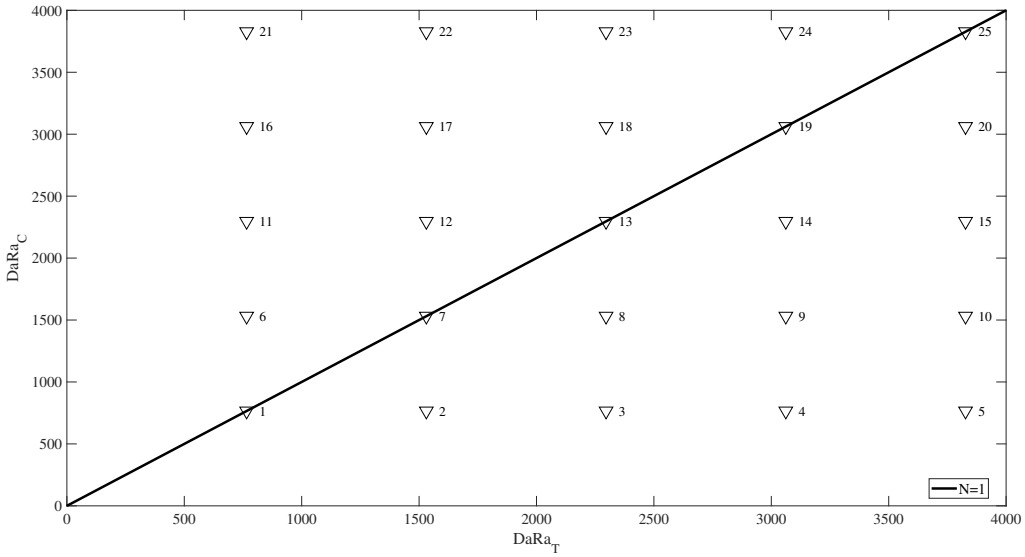



**Figure 3:** Simulation "road-map" for different salinity and temperature combinations expressed in terms of the thermal and saline Rayleigh numbers multiplied by the Darcy number. The solid line corresponds to the equilibrium regime $N \equiv \mathrm{Ra}_C/\mathrm{Ra}_T = 1$. Case numbers (i.e. 1, 2, ... 25) are indicated next to the symbols.

$t$=45 min for cases 3 and 5 are shown in figure 4. Results are scaled using the initial temperature and salinity of the hot and salty fluid, where a value of 1 (dark red) corresponds to $T_1$ or $C_1$, and a value of 0 (dark blue) corresponds to $T_2$ or $C_2$. As seen from figure 4, upper and lower gravity currents propagate faster in case 5 than in case 3 because $|\Delta\rho|$ (and hence the driving force for motion) is larger by a factor of 2. Mimicking observations made for other values of $N < 1$, both cases exhibit significant evidence of fingering, particularly in the salinity field. Fingers, therefore, increase the vertical flux of salt while minimally influencing the temperature field.

To gain additional insights into the flow evolution, the gravity current length was analyzed. In determining buoyant gravity current front positions at each time step, we pinpointed the foremost location at which the density of the hot and salty fluid changed by 5% relative to its initial value. Although a similar kind of analysis was performed vis-a-vis the dense gravity currents, we determined that the gravity currents

**Table 2:** Initial temperature, $T_1$, and salinity, $C_1$, of the hot and salty fluid on the left-hand side of the numerical domain. On the right-hand side of the domain, we consider $T_2 = 293\,\mathrm{K}$ and $C_2 = 0\,\mathrm{mol/m^3}$. All cases share the same Lewis and Darcy numbers, i.e. $\mathrm{Le} = 289$ and $\mathrm{Da} = 2.5 \times 10^{-7}$.

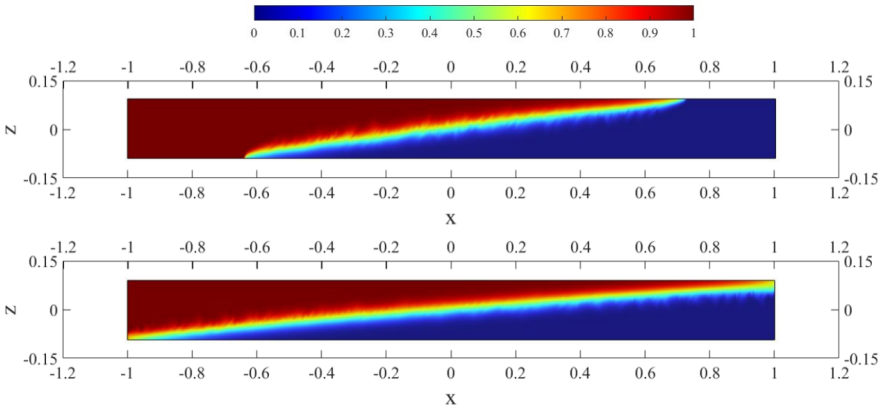
| Case | $T_1$ (K) | $C_1$ (mol/m$^3$) | $\rho_1$ (kg/m$^3$) | $\Delta\rho = \rho_1 - \rho_2$ (kg/m$^3$) | $N$ | $\mathrm{Da}\,\mathrm{Ra}_T$ | $\mathrm{Da}\,\mathrm{Ra}_C$ |
|---|---|---|---|---|---|---|---|
| 1 | 303 | 100 | 1000 | 0 | 1 | 765 | 765 |
| 2 | 313 | 100 | 995 | -5 | 0.5 | 1530 | 765 |
| 3 | 323 | 100 | 990 | -10 | 0.33 | 2300 | 765 |
| 4 | 333 | 100 | 985 | -15 | 0.25 | 3060 | 765 |
| 5 | 343 | 100 | 980 | -20 | 0.2 | 3830 | 765 |
| 6 | 303 | 200 | 1005 | 5 | 2 | 765 | 1530 |
| 7 | 313 | 200 | 1000 | 0 | 1 | 1530 | 1530 |
| 8 | 323 | 200 | 995 | -5 | 0.67 | 2300 | 1530 |
| 9 | 333 | 200 | 990 | -10 | 0.5 | 3060 | 1530 |
| 10 | 343 | 200 | 985 | -15 | 0.4 | 3830 | 1530 |
| 11 | 303 | 300 | 1010 | 10 | 3 | 765 | 2300 |
| 12 | 313 | 300 | 1005 | 5 | 1.5 | 1530 | 2300 |
| 13 | 323 | 300 | 1000 | 0 | 1 | 2300 | 2300 |
| 14 | 333 | 300 | 995 | -5 | 0.75 | 3060 | 2300 |
| 15 | 343 | 300 | 990 | -10 | 0.5 | 3830 | 2300 |
| 16 | 303 | 400 | 1015 | 15 | 4 | 765 | 3060 |
| 17 | 313 | 400 | 1010 | 10 | 2 | 1530 | 3060 |
| 18 | 323 | 400 | 1005 | 5 | 1.33 | 2300 | 3060 |
| 19 | 333 | 400 | 1000 | 0 | 1 | 3060 | 3060 |
| 20 | 343 | 400 | 995 | -5 | 0.8 | 3830 | 3060 |
| 21 | 303 | 500 | 1020 | 20 | 5 | 765 | 3830 |
| 22 | 313 | 500 | 1015 | 15 | 2 | 1530 | 3830 |
| 23 | 323 | 500 | 1010 | 10 | 1.67 | 2300 | 3830 |
| 24 | 333 | 500 | 1005 | -5 | 1.25 | 3060 | 3830 |
| 25 | 343 | 500 | 1000 | 0 | 1 | 3830 | 3830 |

that propagated along the upper and lower boundaries were nearly identical in terms of their lateral propagation. As a result of this up-down symmetry, and for brevity's sake, we restrict attention to the upper gravity currents hereafter.

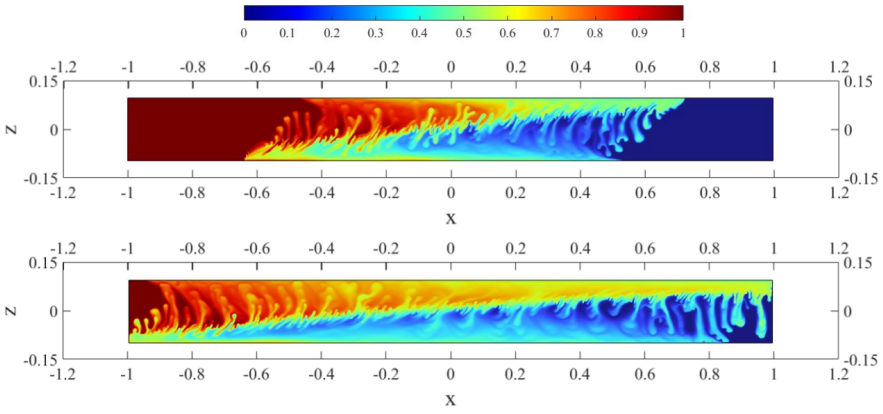
To non-dimensionalise time, the following reference velocity is defined:

$$u_c = \frac{\kappa}{\mu}\Delta\rho_T g\,, \qquad \text{where} \quad \Delta\rho_T = \rho_0\alpha(T_1 - T_2)\,(>0) \tag{23}$$

Here, we prefer using $\Delta\rho_T$ to $\Delta\rho$ because, as table 2 makes clear, the latter density difference is not positive definite. Using $u_c$ as the reference velocity scale and $h$, the domain height, as the reference length scale, a case-dependent time scale is defined to normalize the horizontal axis of figure 5, which shows time series of the gravity current front position for all 10 cases with $N < 1$. Figures such as figure 5 are helpful because they show the similarity in the scaling of the gravity current length of the finger-favorable cases, further emphasizing the importance of the stability ratio as a governing variable of the current setup. To reduce the variations between these different cases and to estimate long-time trends, we consider as the vertical axis variable $l^*_{GC}N^{0.25}$ where $l^*_{GC} \equiv l_{GC}/h$. So normalized, the different curves of figure 5 show a reasonable collapse and a long-time behavior characterized by $l^*_{GC}N^{0.25} \sim t^{*\,0.38}$ where $t^* \equiv t\,u_c/h$. In defining this scaling, note that the exponents 0.25 and 0.38 are determined empirically – to the extent that the values in question may be obtained from a theoretical investigation, we defer consideration to a future investigation.




(a) Temperature




(b) Salinity

**Figure 4:** Normalized temperature and salinity fields after $t = 45$ min for $N < 1$. The upper figures in each panel correspond to case 3 ($N = 0.33$, $\mathrm{Da}\,\mathrm{Ra}_T = 2300$, $\mathrm{Da}\,\mathrm{Ra}_C = 765$), whereas the lower figures correspond to case 5 ($N = 0.2$, $\mathrm{Da}\,\mathrm{Ra}_T = 3830$, $\mathrm{Da}\,\mathrm{Ra}_C = 765$).

## 3.2. Layer-favourable regime

Snapshot images for two layer-favourable cases (i.e. 11 and 21 corresponding, respectively, to $N = 3$ and $N = 5$) are shown in figure 6. Similar to the finger-favourable $N < 1$ cases, increasing the effective Rayleigh number causes the gravity current propagation speed to increase. On the other hand, figure 6 shows that the temperature and salinity fields evolve rather differently for $N > 1$ vs. $N < 1$. To wit, the temperature field lags behind the salinity field, whereas in the finger-favourable regime, temperature and salinity fields propagate downstream at comparable speeds. Under layer-favourable conditions ($N > 1$), the gravity current is driven primarily by the horizontal salinity gradient. As the gravity current elongates, salinity is advected downstream at the gravity current speed. Meanwhile, the evolution of the temperature field is retarded by the requirement that the fluid and solid phases remain in thermal equilibrium. No such restriction applies for salinity: by assumption, salt does not diffuse through the solid phase. Complementing the above explanation, consider (16) and (17), which we solve assuming $\varepsilon = 0.33$ and $G = 1$ [15]. Thus, the relaxation time for heat is approximately three times larger than that for salt. Therefore, in the high Péclet number regimes where diffusion is subordinate to advection, the salinity front propagates three times faster than that associated with temperature. No such difference arises in the finger-favourable regime, where the driving force for fluid motion derives first from temperature differences and second from salinity differences. When $N < 1$, therefore, When $N < 1$, therefore, (i) the salinity front evolves at essentially the same speed as the temperature front: because the buoyancy driving the flow derives principally from the thermal gradient; consequently salinity is advected by the thermally-driven current and cannot advance ahead of the thermal front, (ii) the gravity current front speeds are smaller than those realized when $N > 1$. Contrast, for example, cases 3 and 11, both of which are characterized by $|\Delta\rho| = 10$ kg/m$^3$. From the bottom panel of figure 6, we surmise that the gravity

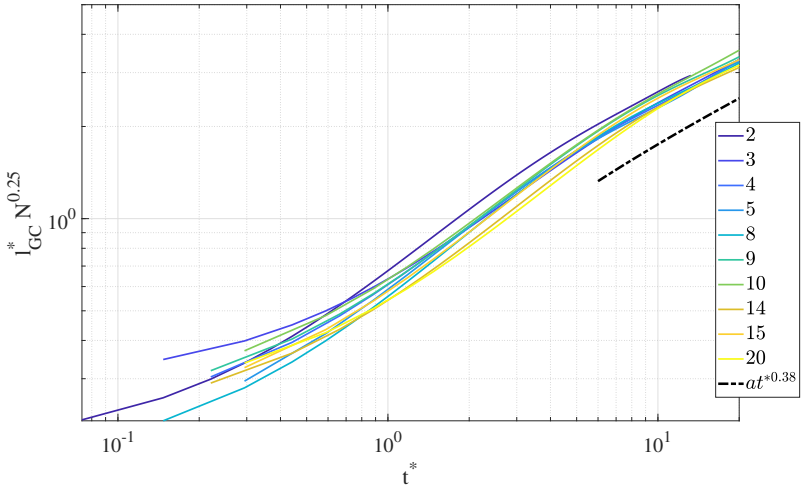



**Figure 5:** Gravity current front position vs. time for the finger-favourable cases, $N < 1$. (Case numbers are as indicated in the legend.) Curves that terminate prematurely indicate scenarios where the gravity current strikes a domain sidewall.

current in the layer-favourable regime has reached the domain boundary; however, the same cannot be said of the gravity current in the finger-favourable regime – see the upper panels of figure 4.

Similar to figure 5, we show a time series of $l^*_{GC}$ in figure 7. In contrast to figure 5, note that (i) the negative values for $l^*_{GC}$ are due to the difference in the propagation direction of the upper gravity currents, which propagate right-to-left; (ii) in non-dimensionalizing the gravity current length, reference is made to a new characteristic front speed, i.e.

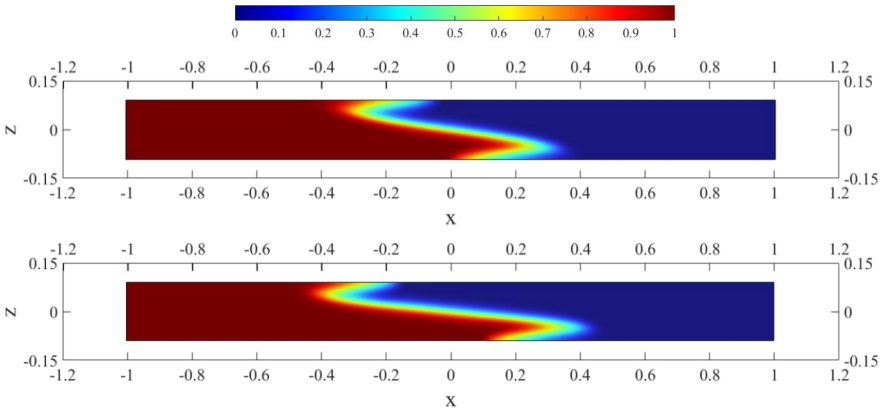
$$u_c = \frac{\kappa}{\mu}\Delta\rho_C g\,, \qquad \text{where} \quad \Delta\rho_C = \rho_0\beta(C_1 - C_2) = \rho_0\beta C_1\ (>0)\,, \tag{24}$$

and, according to the $y$-axis label in figure 7, $l^*_{GC}$ is multiplied by $N^{0.4}$ rather than $N^{0.25}$; (iii) the collapse of curves is not as strong in figure 7 as it is in figure 5; and, (iv) the long-time behavior is described by $l^*_{GC}N^{0.40} \sim t^{*\,0.50}$, not $l^*_{GC}N^{0.25} \sim t^{*\,0.38}$.

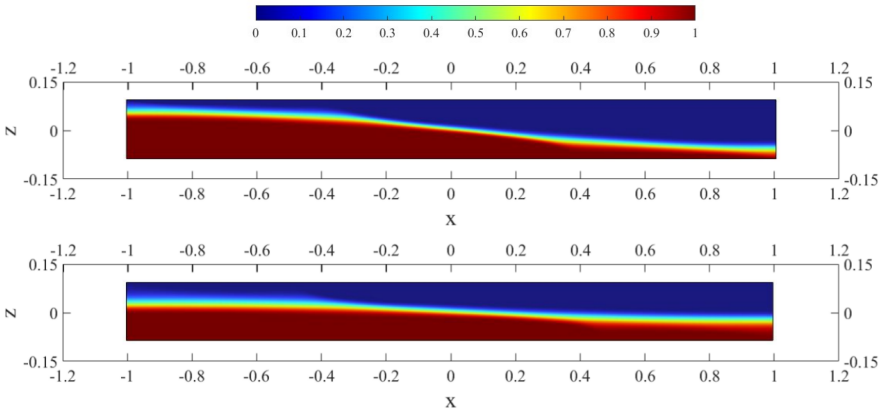
### 3.3. Equilibrium regime

The discussion thus far considers the binary possibilities $N < 1$ and $N > 1$ but says nothing of the intriguing limit $N = 1$ corresponding to cases 1, 7, 13, 19, and 25 and $|\Delta\rho| = 0$. In this "equilibrium regime," reasoning suggests that no gravity current should arise, at least for small $t$. Before studying the equilibrium regime in quantitative detail, we begin by considering double-diffusive dynamics prior to the development of large-scale flow instabilities. At small times, the flow remains in a low Péclet number regime where diffusion, previously considered as small, now dominates. The $10^2$-fold mismatch between $\alpha_e$ and $D_e$ dictates that heat must diffuse faster than salinity. In the vicinity of the vertical interface, therefore, the hot and salty fluid will cool down and become more dense. Meanwhile, the cold and fresh fluid will warm up and become less dense. Although the process is slow by comparison to cases with $N > 1$, the net result is that the hot and salty fluid should flow underneath the cold and fresh fluid, similar to the layer-favourable configurations characterized by $N > 1$. Corroborating this expectation are the upper panels of figure 8 a,b, which show snapshots of the temperature and salinity fields for case 1.

Also included in figure 8 are results for case 25, and here, intriguingly, quite different behaviour is realized. Firstly, the direction of gravity current propagation is not as obvious, particularly when considering the salinity field. Secondly, fingering instabilities arise, whereas they are absent in case 1. The emergence of fingers can be traced back to $t = 0$, and its strong horizontal gradients of heat and salt across the (vertical) interface. The onset and growth of such instabilities in horizontal or even sloping layers experiencing opposing gradients is a well-documented phenomenon that has been much discussed [16, 14]. For instance,




(a) Temperature




(b) Salinity

**Figure 6:** Normalized temperature and salinity fields after $t = 45\,\text{min}$ for $N > 1$. The upper figures in each panel correspond to case 11 ($N = 3$, Da $\text{Ra}_T = 765$, Da $\text{Ra}_C = 2300$)), whereas the lower figures correspond to case 21 ($N = 5$, Da $\text{Ra}_T = 765$, Da $\text{Ra}_C = 3830$))

.

Chen and Chen [3] showed that the flow transitions from quiescent to unsteady convection regimes as the thermal and saline Rayleigh numbers increase. Although the interfaces in our numerical simulations are initially vertical rather than horizontal, we expect similar behaviour here: perturbations to the interface yield localities where hot/salty fluid overlies fluid that is cold/fresh. Fingers therefore develop provided Da $\text{Ra}_T$ = Da $\text{Ra}_C$ is sufficiently large. Thus do we observe fingers in case 25 (Da $\text{Ra}_T$ = Da $\text{Ra}_C$ = 3800) but not in case 1 (Da $\text{Ra}_T$ = Da $\text{Ra}_C$ = 765). It should be noted that no perturbation is explicitly imposed at the interface; the instability is instead seeded by numerical round-off and discretization errors, which supply the infinitesimal disturbances required to trigger fingering once Da $\text{Ra}_T$ = Da $\text{Ra}_C$ exceeds its critical value. A closer inspection of the intermediate cases indicates that this transition occurs between Da $\text{Ra}_T$ = Da $\text{Ra}_C$ = 1530 (case 7), for which no appreciable fingering is observed, and Da $\text{Ra}_T$ = Da $\text{Ra}_C$ = 2300, beyond which fingering becomes pronounced.

The dichotomy between cases 1 and 25 reminds us that two key phenomena govern the equilibrium regime, i.e. (i) diffusion, which increases (decreases) the density of the hot/salty (cold/fresh) fluid, and, (ii) double-diffusive convection, which is responsible for salt rejection from the hot/salty fluid to the cold/fresh fluid. Diffusion and convection thereby bifurcate the flow by creating two (unequal) pairs of counter-flowing gravity currents along the top and bottom boundaries – see figure 9. Along the upper boundary, we label the two gravity currents as $\text{GC}_R$ and $\text{GC}_L$, where the subscript indicates the right vs. left direction of propagation. The diffusion-driven decrease of temperature of hot/salty fluid causes the leftward advection of cold/fresh gravity current fluid along the top boundary, which is labeled as $\text{GC}_L$ in figure 9. Meanwhile, the gravity current labeled as $\text{GC}_R$ is a by-product of initial perturbations to the

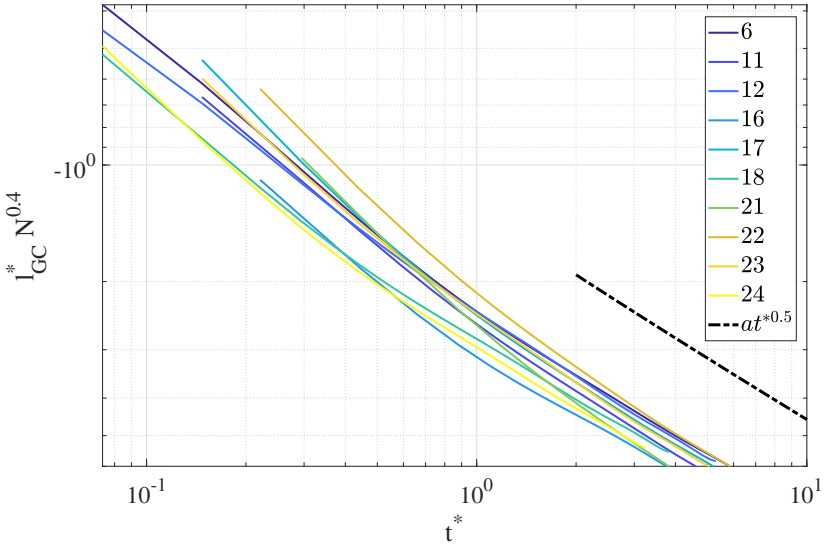
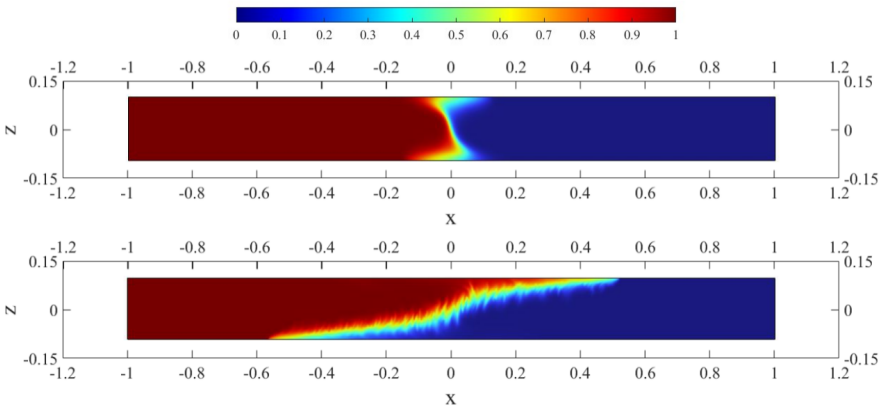
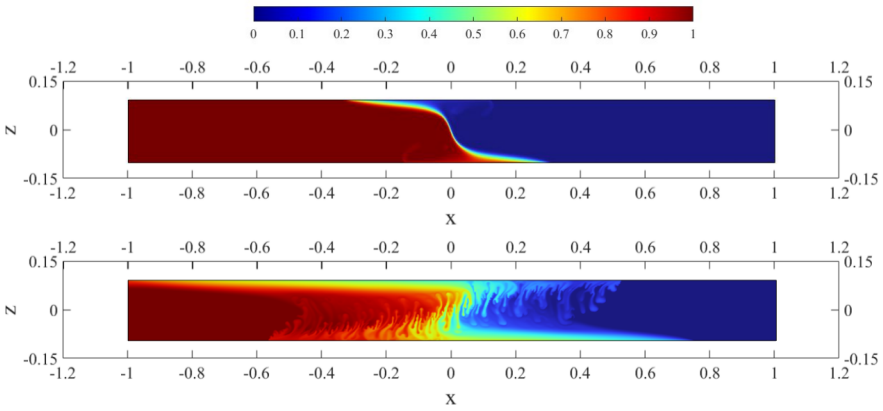



**Figure 7:** Gravity current length for the layer-favourable cases ($N > 1$). (Case numbers are as indicated in the legend.) Curves that terminate prematurely indicate scenarios where the gravity current strikes a domain sidewall.




(a) Temperature




(b) Salinity

**Figure 8:** Normalized temperature and salinity fields after $t = 45$ min for $N = 1$. The upper figures in each panel correspond to case 1 ($\mathrm{Da}\,\mathrm{Ra}_T = 765$, $\mathrm{Da}\,\mathrm{Ra}_C = 765$), whereas the lower figures correspond to case 25 ($\mathrm{Da}\,\mathrm{Ra}_T = 3830$, $\mathrm{Da}\,\mathrm{Ra}_C = 3830$).

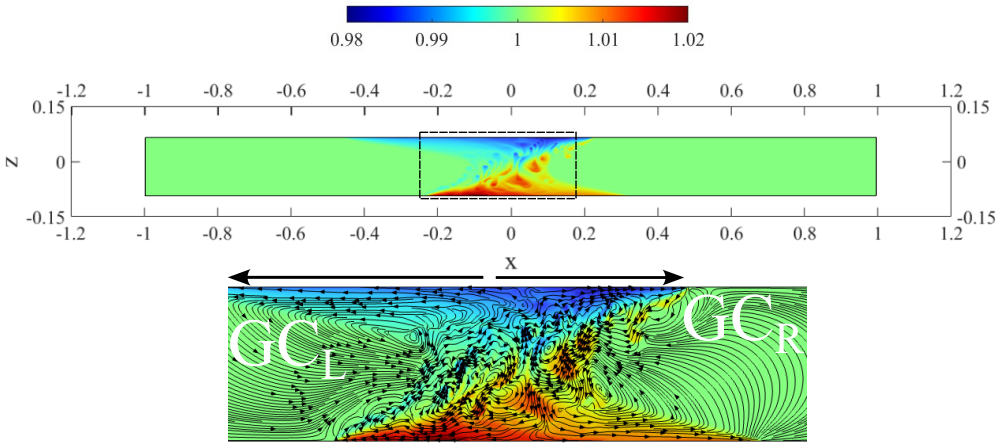



**Figure 9:** Density field and streamlines for case 25 signifying gravity current bifurcation in the equilibrium regime.

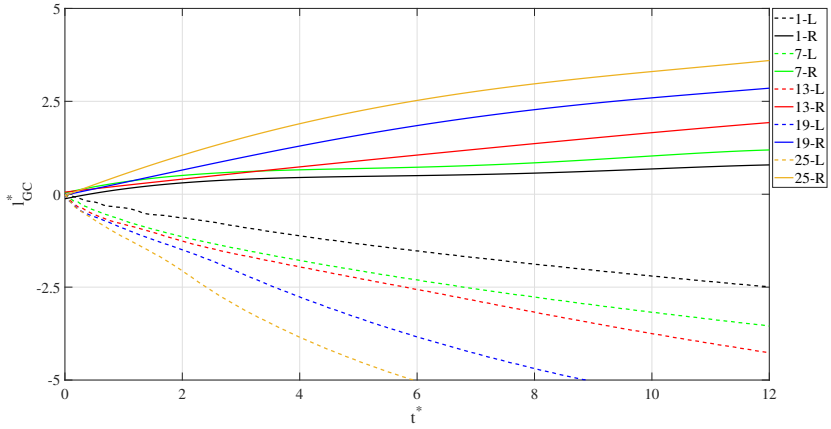



**Figure 10:** Gravity current length for the equilibrium cases ($N = 1$). Case numbers are indicated in the legend where 'R' and 'L' respectively indicate the right vs. left direction of propagation along the upper boundary of the numerical domain.

otherwise vertical interface. Owing to the fingering and salt rejection associated with such perturbations, buoyant fluid rises (falls) to the top (bottom) of the domain, where it spreads laterally, including rightward into cold and fresh fluid.

To characterize the dependency of the left and right gravity currents on the Rayleigh numbers, the gravity current lengths for the five equilibrium cases are shown in figure 10; the dashed lines represent $\mathrm{GC}_L$ and the solid lines represent $\mathrm{GC}_R$. Front speeds are scaled using (23) where $\Delta\rho_T = \rho_0\alpha(T_1 - T_2) = \rho_0\beta(C_1 - C_2) = \Delta\rho_C$ (in the equilibrium regime, $N = 1$ and hence $\alpha(T_1 - T_2) = \beta(C_1 - C_2)$). As shown in figure 10, both $\mathrm{GC}_R$ and $\mathrm{GC}_L$ increase as $\mathrm{Ra}_T = \mathrm{Ra}_C$ increases. Additionally, for cases 25 and 19, the left gravity current strikes the lateral wall just before $t^* = 6$ and $t^* = 9$, respectively. In general, $\mathrm{GC}_L$, which is driven by salinity differences, propagates faster than its right-propagating counterpart, which is driven by temperature differences and is therefore limited by the rate of heat transport through the solid medium.

The difference of front speed for gravity currents driven by differences of salinity vs. temperature can be better appreciated in figure 11. Among all the inset panels shown in figure 11, only that corresponding to case 21 shows gravity currents that reach the lateral walls. Overall, the layer-favourable cases 21 and 11 exhibit a greater gravity current elongation than their analogue finger-favourable counterparts of cases 3 and 5. (Note that $|\Delta\rho_3| = \Delta\rho_{11} = 10$ kg/m$^3$ and $|\Delta\rho_5| = \Delta\rho_{21} = 20$ kg/m$^3$). Moreover, the density

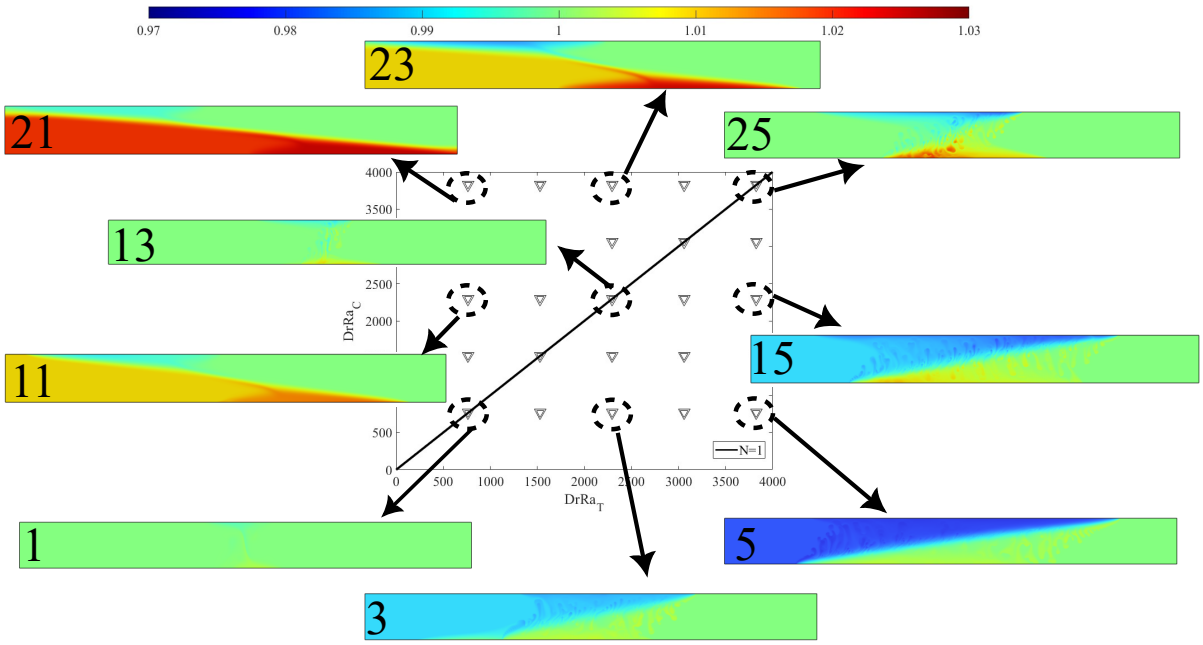



**Figure 11:** Effects of thermal and saline Rayleigh number on gravity current propagation. The inset panels show the normalised density field $\rho/\rho_0$ at $t = 20$ min. Density plots are shown at an earlier time compared to figures 4, 6, and 8 to better highlight the differences between different Rayleigh numbers.

contours for the $N = 1$ cases indicate that mixing severity and gravity current propagation in cases 1 and 13 are relatively weak compared to case 25, where $\mathrm{Ra}_T = \mathrm{Ra}_C$ is larger by comparison.

While it is tempting to draw a qualitative connection between the interleaving thermohaline intrusions described e.g. in Sarkar & Phillips [17, 18] or Chapter 7 of Radko [16] and the flows of figure 11, particularly those corresponding to $N = 1$, we resist this urge for the following reason. Interleaving intrusions have been described mathematically in the context of a background state whose horizontal gradients of temperature and salinity are spatially uniform and constant in time. Because this description does not apply to figure 11, we defer a more detailed investigation of possible connections to future investigations.

### 3.4. Energy budget

The preceding analysis has focused on the evolution of the gravity current front; however, it is equally instructive to apply an energy budget so as to quantify, say, the rate of conversion of potential energy. The energy budget for a Darcy-Boussinesq flow with no-flux boundary conditions can be written as

$$W_D + E_P + W_C = \mathrm{IAE}\,, \tag{25}$$

where

$$W_D = \iint \frac{\mu}{\kappa}\boldsymbol{u}\cdot\boldsymbol{u}\,\mathrm{d}A\,\mathrm{d}t\,, \tag{26}$$

$$W_C = -\iint \frac{\mathrm{D}\rho}{\mathrm{D}t} gz\,\mathrm{d}A\,\mathrm{d}t\,, \tag{27}$$

and

$$E_P = \int_A \rho g z\,\mathrm{d}A\,. \tag{28}$$

Here IAE is the initial available energy, $E_P$ is the potential energy, and $W_D$ is the dissipation. Finally, $W_C$ denotes the conversion of internal energy to potential energy [23]. A complete derivation of the energy budget is provided in Appendix B.

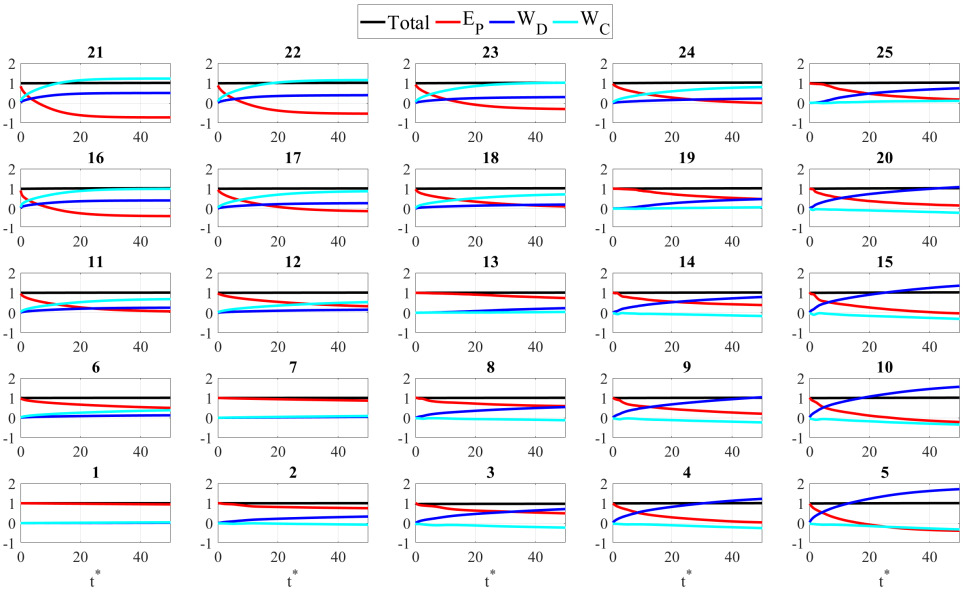



**Figure 12:** Time evolution of the terms from (the normalized analogue of) the energy balance equation – see (25). Case numbers are indicated above each of the sub-figures.

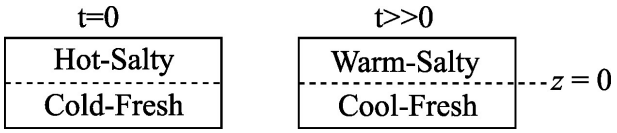
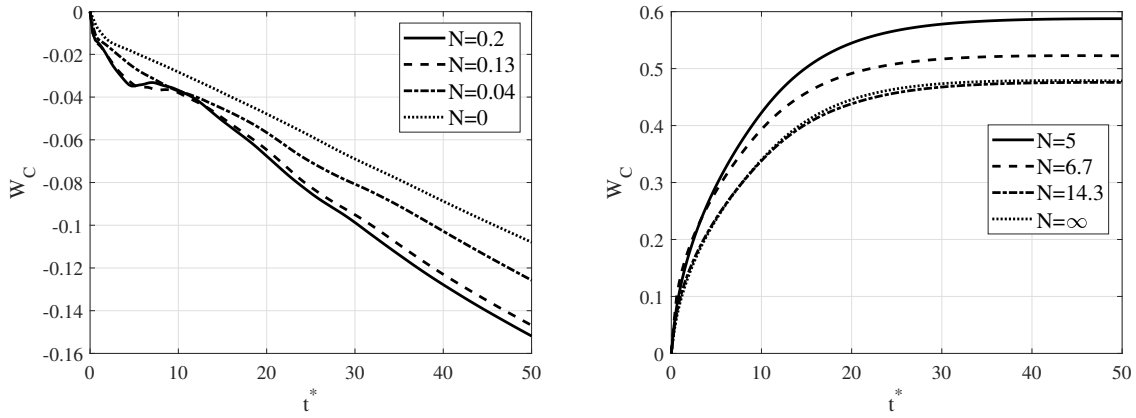



**Figure 13:** Schematic of a hypothetical diffusion-dominated configuration with a horizontal interface.

In interpreting the right-hand side of (25), note that the initial available energy, IAE, is calculated based on the potential energy difference between the initial state and a hypothetical final state in which the upper half of the domain contains the lighter (hot and salty) fluid, whereas the lower half contains the denser (cold and fresh) fluid. This potential energy difference is then multiplied by the square root of the Darcy number to arrive at IAE. For the sake of consistency across all cases, IAE is calculated based on the fluid properties for case 5. The terms in the energy budget have been scaled by IAE to arrive at a normalised analogue to (25). Furthermore, to calculate the time scale, (11) (with $U_f = \frac{\kappa}{\mu}\Delta\rho g$) is utilized with $\Delta\rho$ defined based on the density difference for case 5.

Figure 12 shows the evolution of the terms in the normalised energy budget equation for the 25 cases defined by table 2. Each column of the figure corresponds to isothermal cases having different initial salinities; each row corresponds to isohaline cases having different initial temperatures. Cases on the anti-diagonal correspond to the equilibrium regime $N = 1$, those below the anti-diagonal correspond to the finger-favourable regime $N < 1$, and those above the anti-diagonal correspond to the layer-favourable regime $N > 1$. When $N = 1$, the contribution of $W_C$ to the budget is negligible. Instead, the energy budget is governed by a balance between the dissipation term (increasing) and the potential energy term (decreasing). A similar energy exchange is at play in the finger-favourable $N < 1$ regime; here, however, $W_C$ ($< 0$) can be non-negligible. In case 5, the dissipation term is the largest among all finger-favourable cases, and, by the end of the simulation, $|W_C/W_D| \approx 20\%$. $W_C$ also plays a key role in the layer-favourable cases, where $W_C/W_D > 1$ whenever $N > 1$. Although in the finger-favourable and equilibrium regimes, the energy budget is mostly dictated by a trade-off between $W_D$ and $E_P$, in the layer-favourable case, $W_C$ plays a more substantial role in that $W_C$ accounts for most of the decrease in $E_P$.

The change in sign of the $W_C$ term between the layer- and finger-favourable cases can be better understood by considering a hypothetical state where, instead of a vertical lock gate, the setup consists of a horizontal lock gate where hot and salty fluid is placed over top cold and fresh fluid – see figure 13. Neglecting

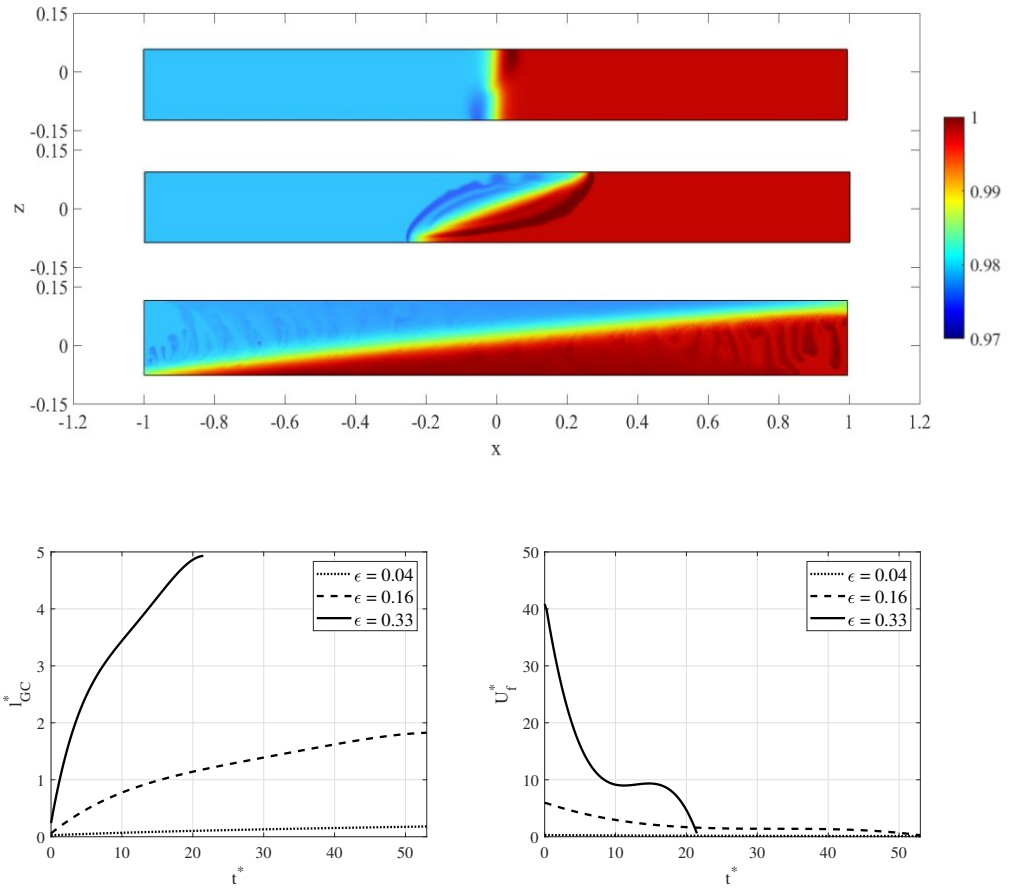



(a) Finger-favourable (b) Layer-favourable

**Figure 14:** Normalised $W_C$ for a range of single-diffusive (dotted line) to strongly double-diffusive (solid line) gravity currents. (a) $N < 1$ and (b) $N > 1$.

convection, imagine a time post-lock-release where the layers have diffused a large amount of heat so that the hot water is now warm and the cold water is now cool; the extent of salt diffusion is limited by comparison. $\mathrm{D}\rho/\mathrm{D}t$ is positive for $z > 0$ and negative for $z < 0$. Either way, $W_C < 0$ – see equation (27). Conversely, in a diffusion-dominated scenario where cold and fresh fluid is placed overtop hot and salty fluid, we expect $W_C$ to be positive. The changes in the sign of $W_C$ are in accordance with the trends in the energy budget: when $N < 1$ (hot and salty fluid overtop of cold and fresh fluid) $W_C < 0$. When $N > 1$, by contrast, (cold and fresh fluid overtop of hot and salty fluid), $W_C > 0$. Although the above conceptual analysis does not account for the effects of convection, Konopliv and Meiburg [9] in their study of high Reynolds number double-diffusive gravity currents demonstrated that convection neither alters the sign of $W_C$ nor significantly modifies its spatial pattern across the single- and double-diffusive cases.

The sign of $W_C$ reflects the stability ratio; however, it does not indicate how double-diffusive convection influences the magnitude of $W_C$. To isolate the dependency of $W_C$ on double diffusion, we consider the dynamics of two single-diffusive configurations, two weakly double-diffusive configurations, two moderately double-diffusive configurations, and two strongly double-diffusive configuration, with the strongly double-diffusive cases corresponding to cases 5 and 21 from before. Simulations were initialized with $|\Delta\rho| = 20\,\mathrm{kg/m^3}$ with different stability ratios. Stability ratios for the finger-favourable simulations ranged from $N = 0$ (single-diffusive) to $N = 0.2$ (strongly double-diffusive). For the layer-favourable simulations, the stability ratio ranged from $N = 5$ (strongly double-diffusive) to $N = \infty$ (single-diffusive). The time evolution of the $W_C$ term for the finger- and layer-favourable regimes is shown in figures 14 a,b, respectively. The results indicate that although double-diffusive convection does not alter the sign of $W_C$, the degree of double-diffusive convection, as quantified by the magnitude of $N$, has a direct influence on the magnitude of $W_C$. In both of the $N > 1$ and $N < 1$ regimes, as the value of the stability ratio shifts from that for a single-diffusive case to a strongly double-diffusive one, the magnitude of $W_C$ increases. This result is expected when $N < 1$ due to the presence of ever more significant fingers as $N$ increases from 0 to 0.2. The explanation is more nuanced, however, when $N > 1$: although $N > 1$ is nominally associated with a layer-favourable regime, we see limited evidence of layer formation in our numerical simulations. A furhter comparison of the differences between the single- vs. double-diffusive gravity currents in the $N > 1$ regime is provided in Section 4.2. There, we will argue that the solid medium is of key importance in understanding the differences in question.




(a) Gravity current length

(b) Gravity front speed

**Figure 15:** Normalized density field $\rho/\rho_0$, gravity current length and front speed for case 5 and three different porosities, $\varepsilon$. The porosity increases from 0.04 to 0.16 to 0.33 from top to bottom in the density field figure, where, in all cases, data are shown at $t^* = 26$.

# 4. EFFECTS OF MEDIUM PROPERTIES

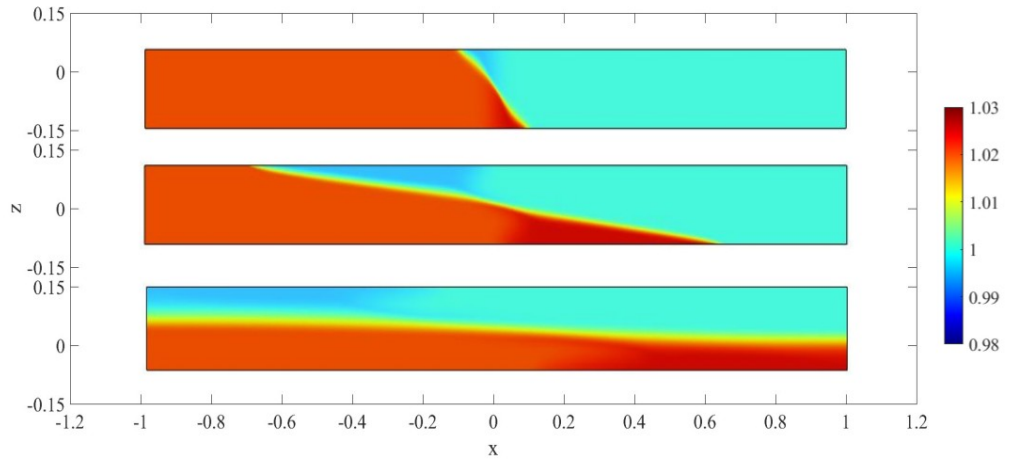
## 4.1. Effects of porosity

The results presented thus far have described how the propagation of the gravity current is affected by the stability ratio and the effective Rayleigh number, but have ignored the influence of permeability and porosity (set to $\varepsilon = 0.33$ above). To investigate the effects in question, we extend the results of the previous section to two additional porosity values, namely $\varepsilon = 0.16$ and $\varepsilon = 0.04$.

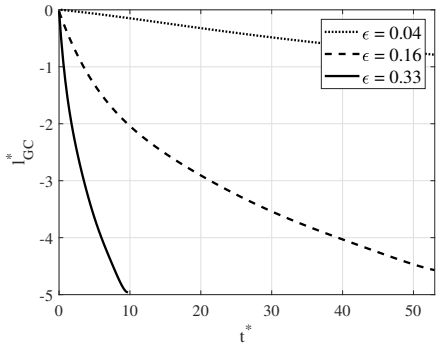
As before, we assume the (uniform) porous matrix to consist of spherical particles so that the Carman-Kozeny equation [13] can be invoked to calculate the permeability, i.e.

$$\kappa = \frac{D_p^2\,\varepsilon^3}{180\,(1-\varepsilon)^2} \tag{29}$$

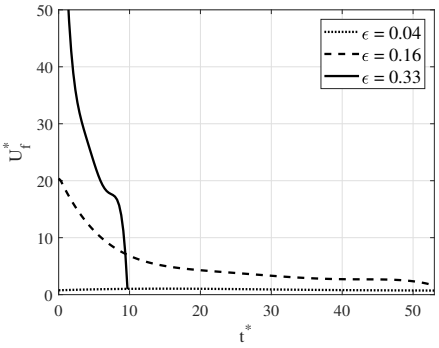
Here $D_p$ is the particle diameter, which, consistent with the original values of porosity ($\varepsilon = 0.33$) and permeability ($\kappa = 10^{-8}\,\mathrm{m}^2$ ), we fix at 4.75 mm. Itis acknowledged that the permeability–porosity relationship of real-world aquifers differs from that expressed in (29); the Carman–Kozeny equation is employed here solely to provide a generic linkage between the variables in question. To examine the effects of porosity, cases 5, 21, and 25 (corresponding to finger-favourable, layer-favourable, and equilibrium regimes with the largest effective Rayleigh numbers) were simulated with the new values for porosity and permeability.




(a) Density




(b) Gravity current length




(c) Gravity front speed

**Figure 16:** Normalized density field $\rho/\rho_0$, gravity current length and front speed for case 21 and three different porosities, $\varepsilon$. The porosity increases from 0.04 to 0.16 to 0.33 from top to bottom in the density field figure, where, in all cases, data are shown at $t^* = 26$.

Figures 15 and 16 show results for the density field, gravity current length, and front speed for cases 5 and 21, respectively. As expected, decreasing the porosity from $\varepsilon = 0.33$ to 0.16 to 0.04 slows down the flow and reduces the gravity current length in both the layer- and finger-favourable regimes. The decrease of porosity and permeability also hinders the onset of instability. While some small-scale fingering is evident when $\varepsilon = 0.16$ in figure 15, there is no discernible indication of fingering when $\varepsilon = 0.04$, primarily because the flow evolution has been so severely impeded.

The connection between porosity and the onset of instabilities is more clearly evident in the results of the equilibrium case – see figure 17. As indicated in the previous subsection, the physics of the equilibrium cases are unique in that oppositely-directed pairs of gravity currents are simultaneously generated: one member of the pair is driven by salinity (diffusion-driven) and the other is driven by temperature (instability-driven). Considering the upper boundary and $\varepsilon < 0.33$, the instability-driven gravity current is practically non-existent in the top two panels of figure 17, resulting in a dominant (left-propagating) gravity current in the upper-half of the domain. The situation is quite different in the lowest panel corresponding to $\varepsilon = 0.33$ where two oppositely-directed gravity currents are evident. Clearly, instability onset is delayed when the medium porosity and permeability are low, and likewise, the effective Rayleigh number. In a free medium, the Rayleigh number alone predicts finger formation; however, in a porous medium, the rate of instability growth is a function of both the Rayleigh and Darcy numbers.

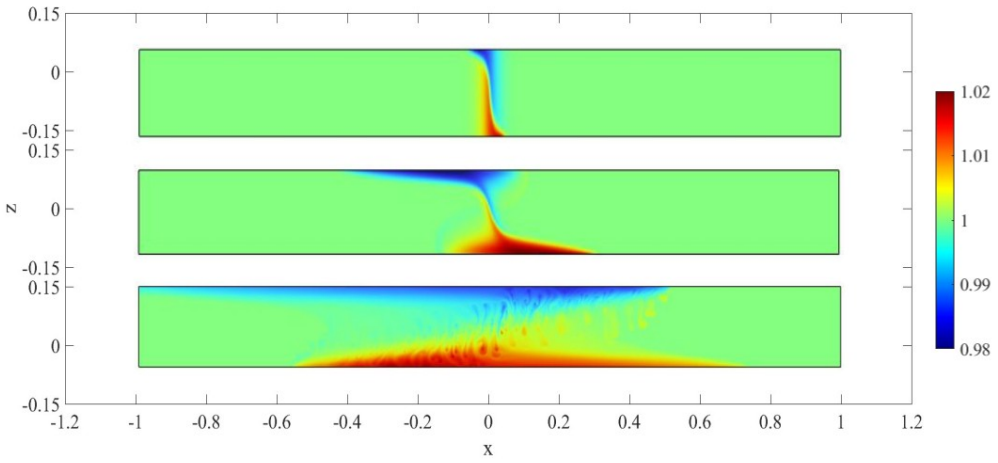



**Figure 17:** Normalized density field, $\rho/\rho_0$, for case 25 at $t^* = 26$ and three different porosities. The porosity increases from 0.04 to 0.16 to 0.33 from top to bottom.

Because reducing $\varepsilon$ and $\kappa$ reduces the Darcy number, the Rayleigh-Darcy number also decreases. When the Rayleigh-Darcy number is especially small, instability onset is curtailed owing to viscous effects.

## 4.2. Effects of the heat capacity ratio

The previous comparison between the gravity current evolution for layer- vs. finger-favourable cases showed that, all else being equal, salinity-driven gravity currents are faster than their thermally driven counterparts due to the ability of the solid medium to entrap heat. Additionally, it was observed that the heat capacity ratio, $G$, is among the factors that appear in the dimensionless governing equations (15 - 17). $G$ prescribes the relaxation time for the temperature field and is therefore analogous to $\varepsilon$, which plays a mathematically similar role for the salinity field. Accordingly, we now define a new variable called the "time-lag", $\phi = \varepsilon/G$, as the ratio between the porosity and the heat capacity ratio, i.e. the ratio between the relaxation times for salt and temperature. Among the key differences between a free medium and a porous medium is the value of the time-lag constant. In the absence of a solid medium, $\phi$, though ambiguous to define, can be set to unity. By contrast, in a porous medium with water as the saturating phase, $\phi < 1$, in general. The time-lag constant is therefore a critical variable, which, as shown below, significantly influences the behavior of the gravity current.

For the set of parameters indicated by table 1, $\phi = 0.33$ and, all else being equal, salinity will adjust approximately three times faster than temperature. To characterize the impact of the time-lag, it is helpful, for comparison's sake, to consider two additional values for the heat capacity of the solid medium, i.e. $c_{psL} = 105$ J/kg.K and $c_{psH} = 4200$ J/kg.K. Thus, we consider $G_L = 0.365$ and $G_H = 1.67$. With $\varepsilon = 0.33$, this yields $\phi_L = 0.9$ and $\phi_H = 0.2$. The closer the value of the time-lag constant to unity (zero), the smaller (larger) the values of the solid heat capacity, $c_{ps}$, and the heat capacity ratio, $G$.

The new values for heat capacity ratio were applied to cases 5 (finger-favourable), 21 (layer-favourable), and 25 (equilibrium regime). For each case, we consider three values of $G$, i.e. low ($L$), medium ($M$), and high ($H$). Normalized density field ($\rho/\rho_0$) results for case 5 at $t = 22.5$ min ($t^* = 13.2$) are shown in figure 18. Evidently, the gravity current length is inversely correlated with $G$. The faster propagation speed observed for small $G$ can be explained as follows: as the heat capacity of the solid phase decreases, the solid retains less of the thermal energy that is, in turn, responsible for driving the gravity current in the finger-favourable regime. As a result, the "damping effects" of the solid medium are reduced. Note also that finger intensity increases with $G$. To place the convective fingers and their associated energy

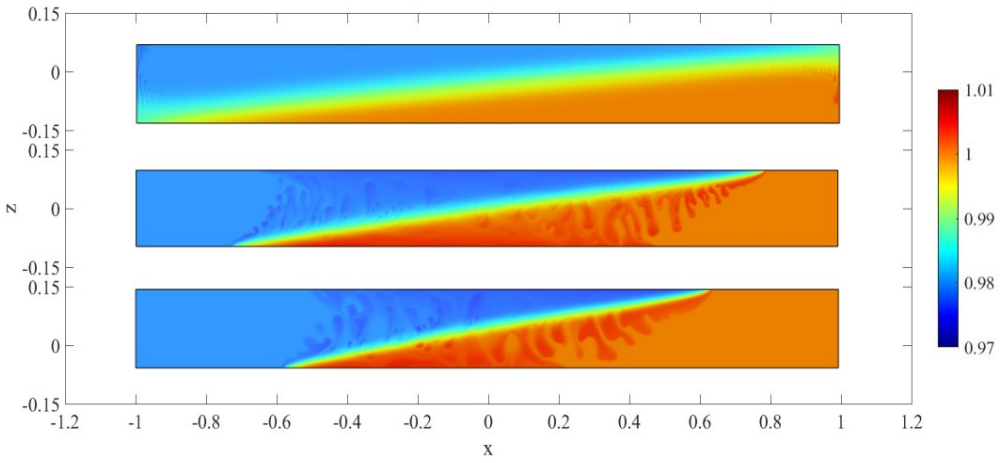



**Figure 18:** Normalized density field for the finger-favourable case 5 with $G_L$=0.365 (top), $G_M$=1 (middle), and $G_H$=1.67 (bottom) at $t^* = 13.2$.

into a quantitative context, we define the average energy flux as

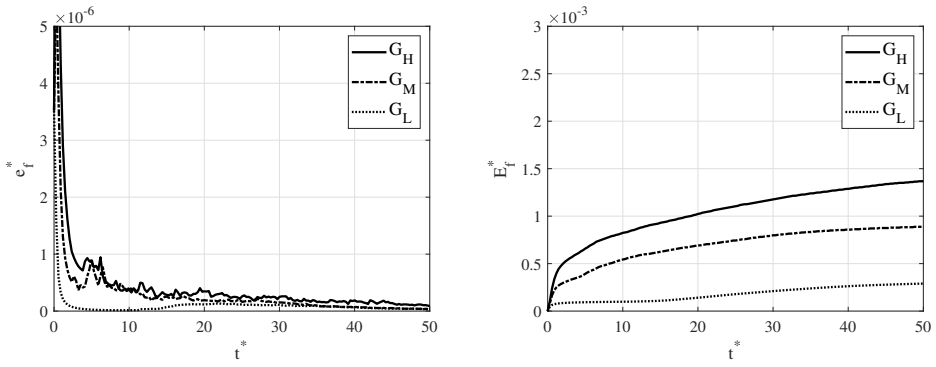
$$e_f^* = \frac{1}{u_c^2}\frac{1}{L}\int_0^L v^2 \, \mathrm{d}L \tag{30}$$

where $L$ is the domain length. Equation (30) calculates the average kinetic energy due to vertical transport by the fingers at the domain midsection located at $z = 0$. In the single-diffusive case, we expect $e_f^*$ to be very close to zero except for a short interval during the initial collapse of the dense fluid into the light fluid. In the presence of a second active scalar, by contrast, the vertical motion induced by the fingers renders $e_f^*$ non-zero and therefore a useful indicator of the severity of the instabilities that form as the flow progresses. Indeed, an even more helpful metric is the time integral of $e_f^*$, defined as

$$E_f^* = \frac{1}{u_c^2}\frac{1}{T}\frac{1}{L}\int_0^T\int_0^L v^2 \, \mathrm{d}L \, \mathrm{d}t \tag{31}$$

where $T$ is the total simulation time. We refer to $E_f^*$ as the cumulative average energy flux. Figure 19 shows results for both $e_f^*$ (panel a) and $E_f^*$ (panel b) and further emphasizes the lack of strong fingering for small $G_L$, i.e. when $G = G_L = 0.365$, $e_f^* \approx 0$ for $5 \leq t^* \leq 13$. Thereafter, weak fingers appear and the dotted line of figure 19 a detaches from the abscissa but remains below the curves corresponding to $G = G_M = 1$ and $G = G_H = 1.67$.

The impact of the heat capacity ratio on the gravity current evolution in the layer-favourable regime (case 21) is illustrated in figure 20. Unlike when $N < 1$, where increasing $G$ decreases the gravity current length, figure 20 exhibits the opposite trend. When $N > 1$, the salinity difference drives the flow. The temperature difference opposes the salinity difference and thereby acts as a "brake." This effect is especially prevalent in a free medium where $\phi = 1$ and $\mathrm{Pe} \gg 1$. The thermal front then propagates at the same speed as the gravity current, and the damping effects associated with temperature differences slow down the gravity current. In a porous medium, by contrast, heat is necessarily partitioned between the fluid and solid. As a consequence, the temperature contrast is less able to oppose the salinity contrast and thereby less able to retard the flow. Heat entrapment in the solid medium can be inferred in the bottom two panels of figure 20, where the density of the right-propagating gravity current increases from $\rho/\rho_0 \simeq 1.02$ to $\rho/\rho_0 \simeq 1.04$ in the streamwise direction corresponding to a chromatic shift from yellow to orange. Meanwhile, the density of the left-propagating gravity current decreases from $\rho/\rho_0 \simeq 1.00$ to $\rho/\rho_0 \simeq 0.98$, corresponding to a chromatic shift from teal to blue. The increase in the density contrast of




(a) Average energy flux (b) Cumulative average energy flux

**Figure 19:** Evolution of the energy associated with the convective fingers at the midsection of the domain for $G_L$=0.365, $G_M$=1, $G_H$=1.67 (case 5).

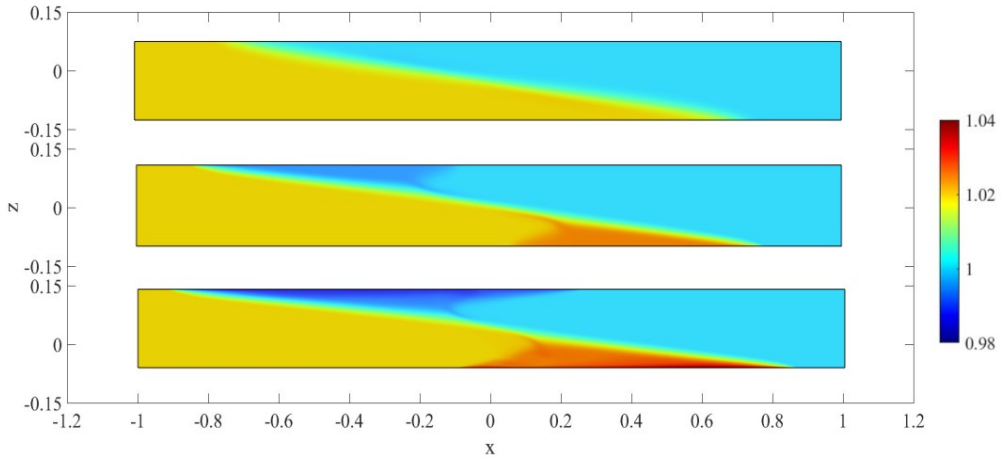
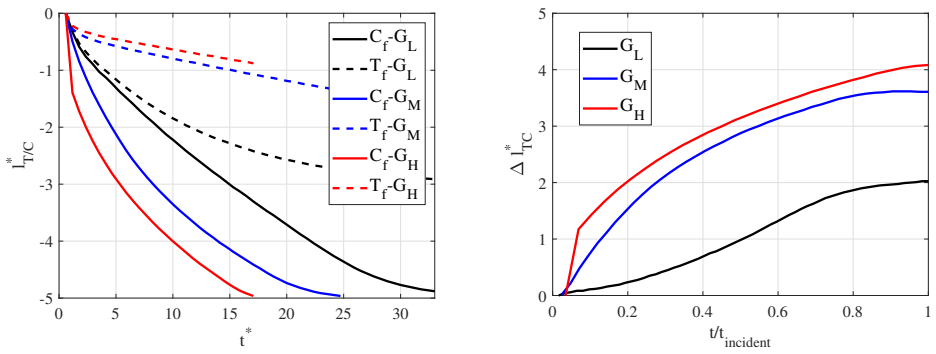



**Figure 20:** Normalized density field for the layer-favourable case 21 with $G_L$=0.365 (top), $G_M$=1 (middle), and $G_H$=1.67 (bottom) at $t^* = 13.2$.

the two currents can also be inferred from figures 6a and 6b, which show the spatial lag of the temperature front vs. the saline front for $G_M$=1.

To measure the spatial lag of the thermal front, we calculate the non-dimensional horizontal position of the saline ($l_C^*$) and thermal fronts ($l_T^*$) for the cold and fresh (i.e. left-propagating) gravity currents shown in figure 20. Results appear in figure 21 a where the solid and dashed lines correspond, respectively, to the saline front ($C_f$) and the thermal front ($T_f$). Qualitatively, the solid and dashed curves both indicate nonlinear elongation with time. Note, however, that the saline front, which, for $N > 1$ defines the gravity current front, advances much more quickly than its thermal counterpart. The disparity is especially pronounced for large $G$. Consistent with this observation, the spatial lag, $\Delta l_{TC}^* = |l_C - l_T|$ shows an increasing trend with $G$ in figure 21 b. Thus, differences between the energy budget of the single- vs. double-diffusive layer-favourable gravity current (previously discussed in Section 3.4) can also be attributed to heat entrapment in the solid medium, which effectively increases the propagation speed of the current. In a porous medium, the differences between single- and double-diffusive gravity current flow are not limited solely to the appearance of instabilities because the flow evolution is influenced by the ability and inability of the solid medium to retain heat and salt, respectively.




(a) (b)

**Figure 21:** (a) Salinity and temperature front positions for $G_L$=0.365, $G_L$=1, and $G_H$=1.67 for the layer-favourable case 21. Solid (dashed) lines represent the saline (thermal) front. (b) Spatial lag, $\Delta l^*_{TC}$, of the salinity vs. temperature front positions for different $G$. Missing data from the initial steps of the simulation causes the kink in the red line for $t \approx 0$. The spatial lag curves were normalized using the case-specific incident time of the gravity current front at the side walls, thereby restricting the analysis to the period before the current reached the lateral boundaries.

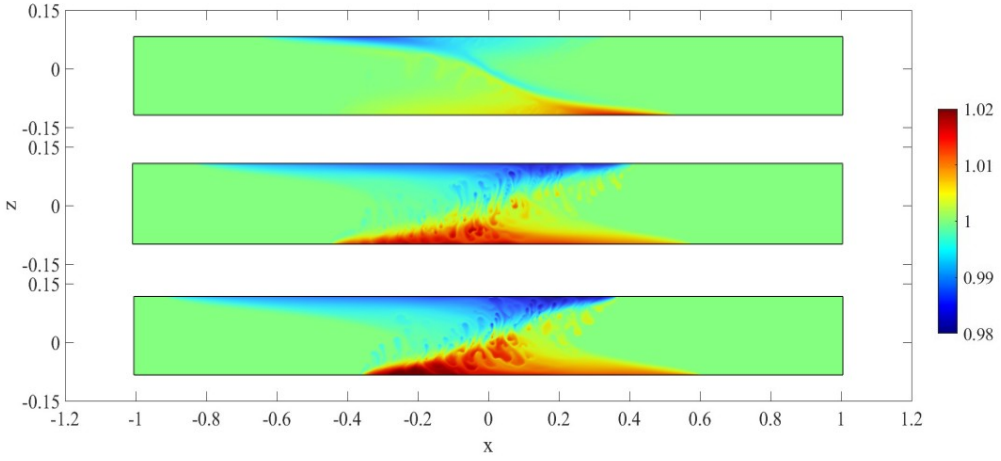



**Figure 22:** Normalized density field for the equilibrium case 25 with $G_L$=0.365 (top), $G_M$=1 (middle), and $G_H$=1.67 (bottom) at $t = 17.8$.

Similar to the $N > 1$ results, the length of the salinity-driven (i.e. left-propagating) gravity current in the equilibrium regime also scales with the heat capacity ratio, as is evident from the normalized density field shown in figure 22. Here, $N = 1$ and the presence of both salinity-driven and thermally-driven currents is expected. When $G = G_L$, however, thermally-driven gravity currents are very faint. In Section 3.3, it was explained that the emergence of the thermally-driven gravity current is due to the instability that develops along the vertical interface for $t = 0^+$. As seen earlier, however, reducing $G$ delays instability onset. The general lack of convective fingers for small $G$ is also evident from the cumulative average energy flux plot of figure 23. In particular, $E^*_f$ remains much smaller in magnitude when $G = G_L$ than for $G = G_M$ or $G = G_H$.

# 5. IMPLICATIONS FOR AQUIFER THERMAL ENERGY STORAGE

The results up to this point have considered the dynamics of double-diffusive gravity currents and how their physics differs from either single-diffusive gravity currents or double-diffusive gravity currents in

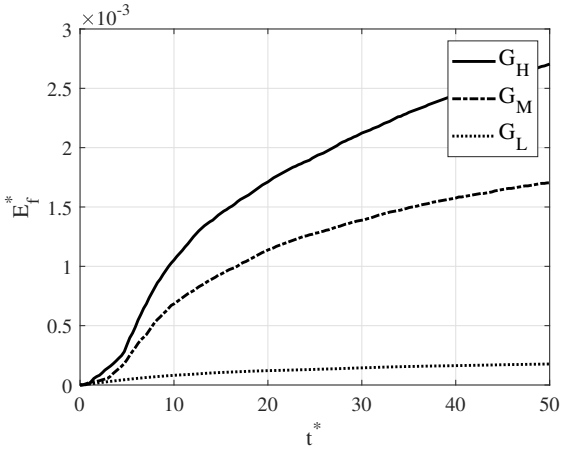



**Figure 23:** Cumulative average energy flux at the midsection of the domain for $G_L$=0.365, $G_M$=1, $G_H$=1.67 for case 25.

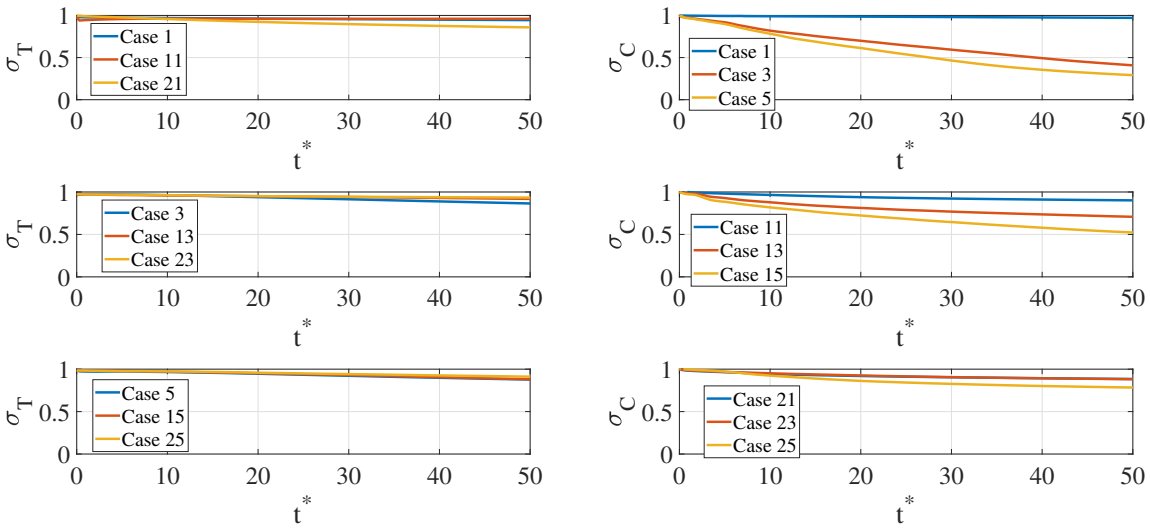
free media. Here, we consider the practicalities of our findings by emphasizing how our simulation results relate to the efficacy of density compensation vis-à-vis aquifer thermal energy storage systems (ATES) [22]. ATES system efficiency is studied in detail by Van Lopik et al. [22], who espoused the benefits of density compensation by which salt is added to the hot water injected into an aquifer so that the injectate density matches that of the resident saturating fluid. In this way, one minimizes buoyancy-driven spread, which can otherwise render the hot fluid more difficult to withdraw when it is later needed e.g. for wintertime district heating. Although Van Lopik et al. [22] demonstrated that applying density compensation can lead to an efficiency increase of around 30%, their results are derived without specific reference to double-diffusive effects. We address this shortcoming here by first quantifying the amount of mixing that occurs for different regimes. We then provide rough guidelines on how to minimize mixing due to convective instabilities. Our approach is motivated by the free medium study of Jha et al. [8] and their quantification of concentration field variance. In a similar manner, and to gain additional insights into the connection between instability formation and mixing, we employ the normalized standard deviations of temperature, $\sigma_T$, and salt, $\sigma_C$, where

$$\sigma_T = \frac{\sqrt{<T^2> - <T>^2}}{T_1}\,, \qquad \sigma_C = \frac{\sqrt{<C^2> - <C>^2}}{C_1}\,. \tag{32}$$

Here, angled brackets indicate the spatial average over the entire numerical domain, and values for $T_1$ and $C_1$ can be found in table 2.

Figure 24 shows the mixing of the temperature (left) and salinity fields (right) for a range of cases from finger-favourable to layer-favourable. In the figure, simulations with similar initial temperatures and concentrations have been grouped together; for instance, cases 1, 11, and 21 (first panel in figure 24a) have an initial temperature of $T_1 = 303$ K, and cases 1, 3, and 5 (first panel in figure 24b) have an initial concentration of $C_1 = 100\,\mathrm{mol/m^3}$. The effects of convective finger formation on the mixing of the salinity field can be seen in the first panel of figure 24b, where finger-favourable cases (cases 3 and 5) show considerably more mixing compared to the equilibrium case (case 1). The larger mixing when $N \leq 1$ is also evident, albeit at a reduced scale, in the results of the temperature field, where finger-favourable cases exhibit a greater overall change of $\sigma_T$ with time than do their layer-favourable counterparts – see e.g. the second panel of figure 24a. The fact that changes to $\sigma_C$ are, in general, larger than changes to $\sigma_T$ is due to the following two factors: (i) vertical transport by the convective fingers is much more effective at transferring salt than heat, and (ii) heat entrapment by the solid medium slows down the advection of the thermal front.

On the basis of the above discussion, it is suggested that a strategy of "over-salting" of the hot fluid is preferable to a strategy of "under-salting." Under-salting the hot fluid results in $N < 1$, where the mixing




(a) $\sigma_T$ (b) $\sigma_C$

**Figure 24:** Mixing of the temperature and salinity fields for different regimes. Cases 1, 13, and 25 correspond to an equilibrium regime, cases 3, 5, and 15 to a finger-favourable regime, and cases 11, 21, and 23 to a layer-favourable regime.

(and lateral spreading) of the temperature field increases due to convective fingering and the consequent acceleration of the gravity current. The same argument even holds true in the equilibrium regime, where extra mixing is anticipated due to instabilities, notably at higher Rayleigh numbers. Whereas "over-salting" is preferable to "under-salting," adding too much salt increases the gravity current front speed, which in turn has a deleterious impact on thermal mixing. It is concluded that a stability ratio slightly greater than unity, corresponding to a weakly layer-favourable regime, is preferable to the fully compensated state ($N = 1$) where mixing is observed to be somewhat more prevalent.

Important to highlight is that the preceding conclusions derive from numerical simulations that, by necessity, were conducted on a domain measuring only $0.2\,\mathrm{m} \times 2\,\mathrm{m}$. By contrast, the (axisymmetric) numerical domain considered by Van Lopik et al. [22] had a radius of 500 m and a height of more than 20 m. A lingering unknown is therefore "Do the small-scale instabilities examined in this work have a demonstrable influence at scales relevant to real ATES systems?" Although further research is necessary to address this vital question, we opine that the answer is more likely yes than no. Indeed, small-scale double-diffusive instabilities have been associated with secondary instabilities of significantly larger dimension, both in porous media (see Sarkar & Phillips [18] and the references therein) and in free media (see Radko [16] and the references therein, particularly those describing collective instability waves, intrusions and thermohaline staircases). If such large-scale secondary instabilities were to form within seasonal timescales, their impact on ATES flow dynamics could, we hypothesize, be substantial.

Also important to highlight is that our numerical simulations consider 2D rather than 3D flows. Again, this is a matter of necessity given the scope of the parametric study that we sought to complete here. Even so, it seems unlikely that qualitatively different conclusions would have followed from 3D numerical output: as noted in the free-medium study of Konopliv and Meiburg [9], fingering is more intense when realized in 3D than in 2D; hence, the estimates of mixing that inform the curves labelled 'Case 3,' 'Case 5,' and 'Case 15' in figure 24 are likely conservative. Detailed numerical work to quantify this conjecture is on-going.

# 6. CONCLUSIONS

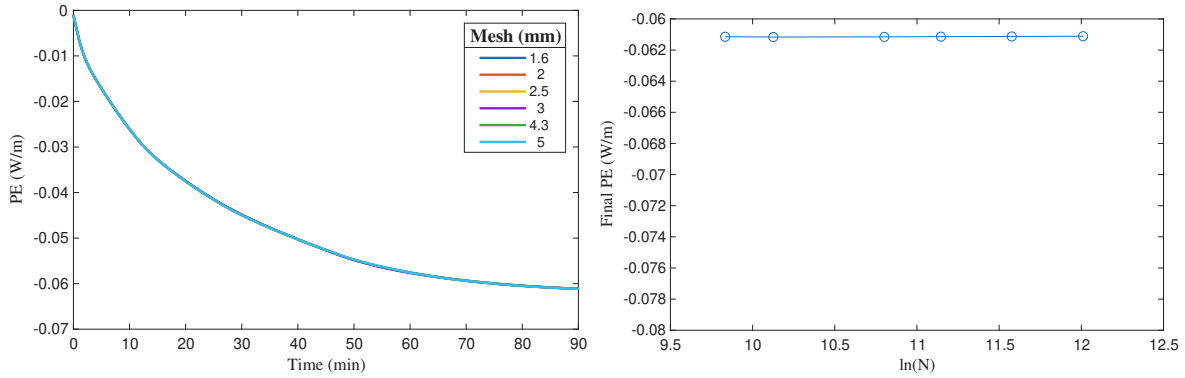
Direct numerical simulations of a double-diffusive lock-exchange flow are conducted to investigate the impact of convective instabilities on the evolution of porous media gravity currents. Numerical results indicate that double diffusion changes the dynamics of the gravity current not only in the finger-favourable regime but also in the layer-favourable regime. The gravity current length is a strong function of the thermal and saline Rayleigh numbers, and the stability ratio, $N$ (defined as the ratio between $\mathrm{Ra}_T$ and $\mathrm{Ra}_C$), governs many of the details of the flow evolution e.g. the severity of the convective fingers that form when $N<1$ – see e.g. figure 4. An investigation of the $N=1$ equilibrium regime further revealed that gravity currents can also form in cases where the density of the hot and salty fluid is fully compensated and so matches that of the cold and fresh ambient fluid. By comparing single- and double-diffusive cases e.g. with respect to the evolution of the terms of the energy budget (25), numerous differences arise. In the $N<1$ finger-favourable regime, differences are attributed to the emergence of convective instabilities, which lead to a more aggressive release of potential energy and faster gravity current propagation speeds. In the layer-favourable $N>1$ regime, differences arise due to the ability of the solid medium to entrap heat but not salt. Thus, we find in figure 20 larger propagation speeds as the specific heat capacity of the solid medium increases, such that the thermal front significantly lags the saline front.

Beyond the solid medium specific heat capacity, its porosity, $\varepsilon$, is likewise a key variable influencing the evolution of the flow. For instance, the horizontal distance traveled by the gravity current decreases with $\varepsilon$. Lower porosity also delays instability onset, thereby reducing the influence of fingering. In this way, decreasing $\varepsilon$ has a qualitatively similar effect to decreasing the specific heat capacity of the solid medium.

Overall, the results of this study suggest that care must be exercised when applying density compensation in ATES systems. While previous work has proposed that system efficiency can be improved by minimizing the density contrast between the injectate and ambient fluid, our results suggest that even in a fully compensated equilibrium regime, significant convective instabilities may still arise. Therefore, we recommend slightly "over-salting" the injectate to avoid the $N<1$ finger-favourable regime and its associated instabilities. All the same, and although the findings of this study provide valuable insight into the practicality of density compensation, the differences between real ATES systems and the simplified lock-exchange configuration exhibited schematically in figure 1 are substantial, and not merely for the difference of length-scale or for the assumption of homogeneous permeability and porosity. Consequently, more advanced numerical simulations coupled with laboratory experiments that account for realistic injection and withdrawal conditions, as well as subsurface heterogeneity, are necessary to more thoroughly quantify the benefits of over- vs. under-salting. Analyses to this effect are ongoing and will be reported upon in follow-up investigations.

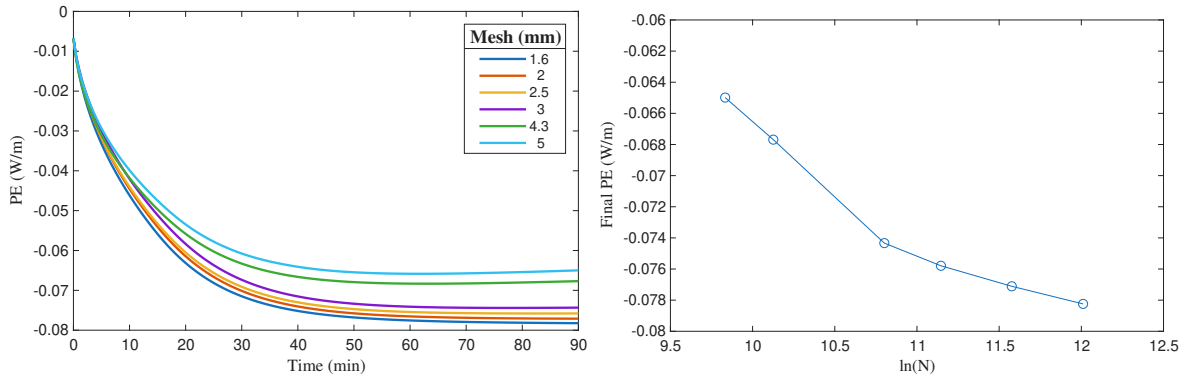
# A. GRID INDEPENDENCE STUDY

To assess grid independence, the Grid Convergence Index (GCI) method was employed. Six grid resolutions with spacings of $[1.6, 2.0, 3.0, 4.3, 5.0]$ mm were used to examine the overall potential energy of the system for cases 5 and 21, which correspond to the highest effective Rayleigh numbers for the finger-favourable and layer-favourable regimes, respectively. The temporal evolution and final values of the potential energy for these cases are shown in figures 25 and 26. For case 5, the evolution of the potential energy exhibits negligible variation across the six grid resolutions, and the final potential energy is the same regardless of grid spacing. By contrast, case 21 shows a monotonic increase in the potential energy as the grid is refined. All the same, the GCI, representing the numerical uncertainty of the simulations, was computed following Celik [2]. The analysis in question yielded values of 0.04% and 1.2% for cases 5 and 21, respectively, thereby confirming the grid-independent nature of the results.




(a) Potential energy vs. time (b) Final potential energy vs. number of grid points

**Figure 25:** Potential energy of case 5 (time-varying and terminal) for six different grid resolutions.




(a) Potential energy vs. time (b) Final potential energy vs. number of grid points

**Figure 26:** Potential energy of case 21 (time-varying and terminal) for six different grid resolutions.

# B. DERIVATION OF THE ENERGY BUDGET EQUATION

The energy budget of a thermohaline gravity current inside a porous medium can be calculated by taking the dot product of (2) with $\boldsymbol{u} = (u,\, v)$, giving

$$\boldsymbol{u}\cdot\boldsymbol{u} = -\frac{\kappa}{\mu}(\boldsymbol{u}\cdot\nabla P + \rho\boldsymbol{u}\cdot\mathbf{g}) \tag{33}$$

Rearranging this last equation and integrating over area yields

$$\int\left(-\frac{\mu}{\kappa}\boldsymbol{u}\cdot\boldsymbol{u}\right)\mathrm{d}A = \int(\boldsymbol{u}\cdot\nabla P)\mathrm{d}A + \int\rho v g\,\mathrm{d}A$$

Using the divergence theorem, mass continuity, and the no-flux boundary condition, it can be shown that the first term on the right-hand side is zero and, as a result, the energy budget simplifies to the following form:

$$\int\left(-\frac{\mu}{\kappa}\boldsymbol{u}\cdot\boldsymbol{u}\right)\mathrm{d}A = \int\rho v g\,\mathrm{d}A \tag{34}$$

Similar to Konopliv and Meiburg [9], we relate the right-hand side term to potential energy, $E_P$, i.e.

$$E_P = \int_A \rho g z\,\mathrm{d}A \tag{35}$$

such that

$$\begin{aligned}\frac{\mathrm{D}E_P}{\mathrm{D}t} &= \int\frac{\mathrm{D}(\rho g z)}{\mathrm{D}t}\,\mathrm{d}A\\ &= \int\left(\frac{\partial(\rho g z)}{\partial t} + \boldsymbol{u}\cdot\nabla(\rho g z)\right)\,\mathrm{d}A\end{aligned} \tag{36}$$

Applying the product rule,

$$\int \left( \frac{\partial(\rho g y)}{\partial t} + \boldsymbol{u} \cdot \nabla \rho g y \right) \mathrm{d}A = \int \left( g y \frac{\partial \rho}{\partial t} + \cancel{\nabla \cdot (\boldsymbol{u} \rho g y)} - \cancel{\rho g y \nabla \cdot \boldsymbol{u}} \right) \mathrm{d}A$$

and consequently

$$\begin{aligned} \frac{\mathrm{D}E_P}{\mathrm{D}t} &= \int \frac{\partial \rho}{\partial t} g z \, \mathrm{d}A \\ &= \int \left( \frac{\mathrm{D}\rho}{\mathrm{D}t} - \boldsymbol{u} \cdot \nabla \rho \right) g z \, \mathrm{d}A \end{aligned} \tag{37}$$

Note, however, that

$$\int (\boldsymbol{u} \cdot \nabla \rho) g z \, \mathrm{d}A = g \int (\cancel{\nabla \cdot (\boldsymbol{u} \rho z)} - \rho \nabla \cdot (\boldsymbol{u} z)) \, \mathrm{d}A \tag{38}$$

and therefore

$$\begin{aligned} \int (\boldsymbol{u} \cdot \nabla \rho) \, g z \, \mathrm{d}A &= g \int \big( - \rho \, \nabla \cdot (\boldsymbol{u} z) \big) \, \mathrm{d}A \\ &= g \int (-\rho v - \cancel{\rho z \nabla \cdot \boldsymbol{u}}) \, \mathrm{d}A \end{aligned}$$

Thus do we arrive at

$$\frac{\mathrm{D}E_P}{\mathrm{D}t} = \int \frac{\mathrm{D}\rho}{\mathrm{D}t} g z \, \mathrm{d}A + \int \rho v g \, \mathrm{d}A \tag{39}$$

By coupling (34) and (39) and then integrating the energy budget in time, the final form is obtained, i.e.

$$\frac{\mathrm{D}E_P}{\mathrm{D}t} + \int \frac{\mu}{\kappa} \boldsymbol{u} \cdot \boldsymbol{u} \, \mathrm{d}A - \int \frac{\mathrm{D}\rho}{\mathrm{D}t} g z \, \mathrm{d}A = 0 \tag{40}$$

$$E_P + \iint \frac{\mu}{\kappa} \boldsymbol{u} \cdot \boldsymbol{u} \, \mathrm{d}A \, \mathrm{d}t - \iint \frac{\mathrm{D}\rho}{\mathrm{D}t} g z \, \mathrm{d}A \, \mathrm{d}t = \text{constant} \tag{41}$$

## Author Contributions

**K RahnamayBahambary**: Conceptualization, Investigation, Methodology, Software, Visualization, Writing - original draft. **Tarun K. Jain**: Conceptualization, Investigation, Software, Visualization,- Review & Editing. **Chunendra K. Sahu**: Conceptualization, Methodology,- Review & Editing. **M. R. Flynn**: Conceptualization, Project administration, Funding acquisition, Investigation, Supervision- Review & Editing.

## Conflicts of Interest

All four authors declare that they have no conflict of interest.

## Data, Code & Protocol Availability

The data that support the findings of this study are available from the corresponding author upon reasonable request.

## Funding Received

Major funding for this project was generously provided by NSERC through the Discovery Grant and Alliance Grant programs. Additional funding was contributed by U. Alberta through the Energy Transition Seed Grant Program.

## ORCID IDs

K RahnamayBahambary https://orcid.org/0000-0003-0167-4878
Tarun K. Jain https://orcid.org/0009-0004-3278-1259
Chunendra K. Sahu https://orcid.org/0000-0003-2003-8607
M. R. Flynn https://orcid.org/0000-0002-7559-9463

# REFERENCES

1. Stijn Beernink, Niels Hartog, Philip J. Vardon, and Martin Bloemendal. Heat losses in ates systems: The impact of processes, storage geometry and temperature. *Geothermics*, 117:102889, 2024. ISSN 0375-6505. .
2. Ismail B. Celik. Procedure for estimation and reporting of uncertainty due to discretization in CFD applications. *Journal of Fluids Engineering*, 130(7):078001, 07 2008. ISSN 0098-2202. .
3. Falin Chen and C.F. Chen. Double-diffusive fingering convection in a porous medium. *International Journal of Heat and Mass Transfer*, 36(3):793–807, February 1993. ISSN 00179310. .
4. David Geerts, Alexandros Daniilidis, Gert Jan Kramer, Martin Bloemendal, and Wen Liu. Analytically estimating the efficiency of high temperature aquifer thermal energy storage. *Geothermal Energy*, 13(1):17, 2025. ISSN 2195-9706. .
5. R. W. Griffiths. Layered double-diffusive convection in porous media. *Journal of Fluid Mechanics*, 102: 221–248, 1981. .
6. N. Hadidi and R. Bennacer. Three-dimensional double diffusive natural convection across a cubical enclosure partially filled by vertical porous layer. *International Journal of Thermal Sciences*, 101:143–157, March 2016. ISSN 12900729. .
7. G M Homsy. Viscous fingering in porous media. *Annual Review of Fluid Mechanics*, 19(Volume 19, 1987): 271–311, 1987. ISSN 1545-4479. .
8. Birendra Jha, Luis Cueto-Felgueroso, and Ruben Juanes. Fluid mixingm from viscous fingering. *Physical Review Letters*, 106(19):194502, May 2011. ISSN 0031-9007, 1079-7114. .
9. Nathan Konopliv and Eckart Meiburg. Double-diffusive lock-exchange gravity currents. *Journal of Fluid Mechanics*, 797:729–764, June 2016. ISSN 0022-1120, 1469-7645. .
10. P. F. Linden. Convection in the environment. In G. K. Batchelor, H. K. Moffatt, and M. G. Worster, editors, *Perspectives in Fluid Dynamics: A Collective Introduction to Current Research*, pages 289–345. Cambridge University Press, Cambridge, 2000. ISBN 9780521792744.
11. N. Mimouni, R. Bennacer, S. Chikh, and O. Rahli. Limitation of parallel flow in double diffusive convection: Two- and three-dimensional transitions in a horizontal porous domain. *Physics of Fluids*, 26(7):074105, July 2014. ISSN 1070-6631, 1089-7666. .
12. B. T. Murray and C. F. Chen. Double-diffusive convection in a porous medium. *Journal of Fluid Mechanics*, 201:147–166, 1989. .
13. D. A. Nield and A. V. Kuznetsov. A historical and topical note on convection in porous media. *Journal of Heat Transfer*, 135(6):061201, June 2013. ISSN 0022-1481, 1528-8943. .
14. Donald A. Nield and Adrian Bejan. *Convection in Porous Media*. Springer International Publishing, 2017.
15. O. M. Phillips. *Flow and Reactions in Permeable Rocks*. Cambridge University Press, Cambridge, 1991.
16. Timour Radko. *Double-Diffusive Convection*. Cambridge University Press, 2013.
17. A. Sarkar and O. M. Phillips. Effects of horizontal gradients on thermohaline instabilities in infinite porous media. *J. Fluid Mech.*, 242:79–98, 1992.
18. A. Sarkar and O. M. Phillips. Effects of horizontal gradients on thermohaline instabilities in a thick porous layer. *Phys. Fluids*, 4:1165–1175, 1992.
19. R W Schmitt. Double diffusion in oceanography. *Annual Review of Fluid Mechanics*, 26(Volume 26, 1994): 255–285, 1994. ISSN 1545-4479. .
20. William D. Smyth and Jeffrey R. Carpenter. *Convective Instability*, page 24–52. Cambridge University Press, 2019.
21. J S Turner. Double-diffusive phenomena. *Annual Review of Fluid Mechanics*, 6(Volume 6, 1974):37–54, 1974. ISSN 1545-4479. .
22. Jan H. Van Lopik, Niels Hartog, and Willem Jan Zaadnoordijk. The use of salinity contrast for density difference compensation to improve the thermal recovery efficiency in high-temperature aquifer thermal energy storage systems. *Hydrogeology Journal*, 24(5):1255–1271, August 2016. ISSN 1431-2174, 1435-0157. . Publisher: Springer Science and Business Media LLC.
23. Kraig B. Winters, Peter N. Lombard, James J. Riley, and Eric A. D'Asaro. Available potential energy and mixing in density-stratified fluids. *Journal of Fluid Mechanics*, 289:115–128, April 1995. ISSN 0022-1120, 1469-7645. .

683 24. Erik Witter, Patrick Dobson, Dayo Akindipe, Joshua McTigue, Trevor Atkinson, Ram Kumar, Eric
684 Sonnenthal, and Guangdong Zhu. A review of geological thermal energy storage for seasonal, grid-scale
685 dispatching. *Renewable and Sustainable Energy Reviews*, 218:115761, 2025. ISSN 1364-0321. .